



# Finite Element Analysis of Low-Speed Oblique Impact Behavior of Adhesively Bonded Composite Single-Lap Joints

M. Gokhan Atahan<sup>1</sup> · M. Kemal Apalak<sup>2</sup>

Received: 31 May 2022 / Accepted: 9 March 2023 / Published online: 14 April 2023  
© The Author(s), under exclusive licence to Springer Nature B.V. 2023

## Abstract

The development of a realistic numerical model that predicts the impact behavior of adhesively bonded composite joints is important for many industrial sectors such as automotive, aerospace, and marine. In this study, it was aimed to develop a numerical model that can predict the low-velocity oblique impact behavior of composite single-lap joints close to the experimental results. The validation of the proposed numerical model was carried out with the results of the previously experimentally tested joints. In explicit finite element analysis, the orthotropic material model and Hashin's damage criterion were used in the numerical model of composite adherends. The adhesive region was divided into three different regions. The cohesive zone model (CZM) was used to determine the damage initiation and propagation in the upper and lower interface regions of adhesive. The middle region of the adhesive between the two cohesive interfaces was modeled with an elastic–plastic material model to reflect the plastic material behavior of the adhesive in the analysis. The effects of impact angle, fiber orientation, and overlap length on adhesive damage initiation and propagation were investigated in detail. There is a good agreement between the numerical and experimental results, considering the contact force-time variations and composite and adhesive damage. The impact angle and fiber angle had a significant effect on the impact behavior of the composite joints and the adhesive damage initiation and propagation. The increase in impact angle and fiber angle caused a decrease in the maximum contact force value. Adhesive damage propagation patterns varied according to the composite fiber orientation. In addition, since the shear toughness of the adhesive is higher than its tensile toughness, the amount of adhesive damage and damage propagation rate decreased as the impact angle increased.

**Keywords** Low speed impact · Oblique impact · Cohesive zone model · Finite element method · Single-lap joint

## Acronyms and Nomenclature

*LEFM* Linear elastic fracture mechanics  
*MMF* Mixed-mode flexure

---

✉ M. Gokhan Atahan  
mithatgokhan.atahan@agu.edu.tr

<sup>1</sup> Department of Mechanical Engineering, Abdullah Gul University, Kayseri 38080, Turkey

<sup>2</sup> Department of Mechanical Engineering, Erciyes University, Kayseri 38030, Turkey

<i>CZM</i>	Cohesive zone model
<i>SDEG</i>	Scalar stiffness degradation variable
<i>DAMAGEFT</i>	Fiber tensile damage variable
<i>DAMAGEFC</i>	Fiber compressive damage variable
<i>DAMAGEMT</i>	Matrix tensile damage variable
<i>DAMAGEMC</i>	Matrix compressive damage variable
<i>DAMAGESHR</i>	Matrix shear damage variable
<i>E</i>	Modulus of elasticity
<i>G</i>	Shear modulus
<i>v</i>	Poisson's ratio
$X^T$	Longitudinal tensile strength
$X^C$	Longitudinal compressive strength
$Y^T$	Transverse tensile strength
$Y^C$	Transverse compressive strength
$S^L$	Longitudinal shear strength
$S^T$	Transverse shear strength
$G_{ft}^c$	Fiber tensile fracture energy
$G_{fc}^c$	Fiber compressive fracture energy
$G_{mt}^c$	Matrix tensile fracture energy
$G_{mc}^c$	Matrix compressive fracture energy
$t_n$	Cohesive traction in tension
$t_{s,t}$	Cohesive tractions in shear
$\delta_n$	Cohesive separation in tension
$\delta_{s,t}$	Cohesive separations in shear
<i>D</i>	Damage parameter
$\alpha$	Non-dimensional damage parameter
$\delta_f^o$	Effective interfacial separation at failure initiation
$\delta_m^p$	Effective interfacial separation at failure
$\delta_m^{max}$	Effective interfacial separation at complete failure

## 1 Introduction

Composite materials are widely used in the automotive and aerospace industry due to allow lightweight and high-strength structures [1, 2]. In engineering structures, there is a need to combine composite materials with similar or dissimilar materials. Adhesive joints are widely preferred in joining composite materials, as adhesive joints allow uniform stress distribution, ease of application, and joining of dissimilar materials [3–5]. Adhesive joints may be exposed to static and dynamic loads in engineering applications. For this reason, the behavior of the adhesive joints under static load as well as under dynamic load should be taken into account in the design of the joints. Due to the inertia effect, the behavior of the joints under impact load differs from the behavior under static load [5].

In the automotive industry, joints are exposed to out-of-plane impact loads. For this reason, automotive engineers consider the oblique impact (side-impact and pillar impact) effect in joint design [6]. In addition, damage analysis of adhesively bonded joints subjected to transverse impact load is an important issue to consider in the design of adhesively bonded structures [7]. Determining the behavior of adhesive joints under impact load is a very complex and difficult task. One of the reasons is that it requires expensive

and highly sensitive experimental testing components. Another reason is that the mechanical behavior of the adherend and adhesive materials under dynamic load may differ from the behavior under static load [5]. The finite element method allows examination of the effect of many design parameters on the impact behavior of the joints. For this reason, a numerical model of adhesively bonded joints that provides results close to the experimental results saves time and costs, as well as detects some situations that are difficult to determine experimentally, such as time-dependent adhesive damage propagation.

In the adhesive numerical model, the CZM is widely preferred to predict the mechanical behavior of the joints under static and dynamic loads. The CZM theory is based on Linear Elastic Fracture Mechanics (LEFM) [8]. The CZM can reflect the elastic and damage behavior of very small interfaces in the model without any numerical errors. One of the most important advantages of the CZM is that it provides a gradual degradation of material stiffness, allowing for the determination of the initiation and propagation of damage. Moreover, it provides the detection of multiple damage mechanisms by taking into account the normal and shear tractions.

The mechanical behavior of adhesively bonded joints under in-plane impact loading has been investigated by many researchers [9–13]. They used different material model approaches for adhesive and adherends in the numerical model of adhesively bonded joints. Hazimeh et al. [9] studied the geometric and material effects on the composite double-lap joint under dynamic in-plane load. Elastic behavior was preferred in the numerical material model of adhesive and adherends. Machado et al. [10] developed a numerical model simulating the behavior of composite mixed adhesive joints under in-plane quasi-static and impact loads. While the orthotropic material model was preferred for composite adherends, the CZM was used in the adhesive, and the region of composite adherends close to the adhesive. They found that the difference between numerical and experimental results under impact load was greatest for joints containing flexible adhesives. Morgado et al. [11] developed a numerical model to examine the performance of adhesively bonded composite single-lap joints under quasi-static and impact loads. While the elastic behavior of the composite adherends was described by the orthotropic material model, the CZM was used in the regions close to the adhesive to detect the delamination failure. They predicted the joint behavior and damage mechanism close to the experimental results under both quasi-static and impact loads with the used material model. Machado et al. [12] numerically investigated the behavior of similar and dissimilar single-lap joints manufactured with composite and aluminium under in-plane quasi-static and impact loads. The CZM was used to determine the adhesive damage and the composite delamination. There was a linear relationship between joint performance and overlap length, which was valid for overlap lengths between 12.5 and 50 mm. Peres et al. [13] studied the effect of overlap length and adhesive type on the strength of composite single-lap joints under impact load through the CZM. The numerical model predicted the impact strength of the joints with good accuracy and the increase in overlap length increased the joint strength.

Under the in-plane impact load, the adhesive region is subjected to predominantly shear stresses, while under the out-of-plane impact (transverse impact) load, it is subjected to normal and shear stresses. Therefore, the mechanical behavior and damage mechanism of adhesively bonded joints develop differently under out-of-plane impact. For joint design, it is important to determine the in-plane impact behavior of adhesive joints as well as the out-of-plane impact behavior. Many studies were performed on the out-of-plane impact behavior of adhesively bonded joints [6, 7, 14–19].

Chen et al. [6] experimentally and numerically investigated the behavior of thermo-plastic single-lap double riveted joints with and without adhesive under out-of-plane

impact and quasi-static concentrated loading. Elastic behavior in composite adherends was described by the orthotropic material model and the adhesive material model was defined with the CZM. They noted that the adhesive rivet joint had a higher stiffness before debonding initiation and the peak load of the adhesive rivet joint was 7–20% lower than the joint without adhesive for the same impact energy level. He and Pan [7] studied the damage analysis of adhesively bonded composite-titanium single-lap joints under transverse projectile impact. They examined the failure mechanism of joints with two damage models. They determined adhesive-adherend interface debonding damage using the CZM and composite damage using Hashin's criterion and continuum damage mechanics. In the adhesive region, the CZM was used for the interface, while the elastic–plastic material model was preferred for the remaining part of the adhesive layer. In this way, the plastic behavior of the adhesive was reflected in the numerical analysis. They determined the damage modes as local debonding in the adhesive-titanium adherend interface, matrix cracking in the composite adherend and global debonding in the adhesive-titanium adherend interface under increasing impact load. Huang et al. [16] investigated the low-energy impact damage and post-impact fatigue behavior of adhesively bonded composite/steel and composite/composite single-lap joints. The linear elastic material model and Hashin's Damage Criterion were used for composite adherends and the CZM was preferred for the adhesive numerical model. The adhesive layer of the composite/steel joints was more effective in lower energy impact compared with the composite/composite joints. Liu and Yan [17] investigated the damage mechanism of adhesively bonded composite scarf repairs for different impact locations. They determined the adhesive damage initiation and propagation with the CZM. The highest adhesive damage level occurred in the middle of the joint, the damage initiated below the impact point, and propagated towards the free edge. Erbayrak [18] studied the low-velocity impact behavior of dissimilar single-lap joints using the CZM. The numerical results were in good agreement with the experimental results due to the modeling of the adhesives using the proper CZM, the application of suitable boundary conditions, and the preference of the suitable contact type in the impact analysis. Boling and Dongyun [19] analysed the dynamic behavior of adhesively bonded composite-titanium single-lap joints using the three-dimensional finite element method. The elastic–plastic material model was used in the numerical model of titanium adherend and adhesive. They determined that the compressive stress occurred its highest value at the beginning of the impact phenomena, while the tensile stress occurred at its highest value after a period of impact time in the joint under out-of-plane impact load.

Considering the literature survey, it was seen that studies on the impact behavior of adhesive joints have increased recently and their dynamic behavior under out-of-plane impact load as well as in-plane impact load has been examined. However, it was determined that studies on out-of-plane impact generally concentrate on the behavior of joints under transverse normal impact. Therefore, examining the oblique impact load effect on joint behavior will provide an important design parameter for adhesive joints. In previous studies, the behavior of aluminium single-lap joints under normal impact load was examined [20, 21]. The effect of the plastic deformation ability of the adherends on the initiation and propagation of adhesive damage was investigated. The effect of the plastic deformation ability of the adherends on the impact behavior of the joint was determined by using aluminium adherends with two different mechanical properties. Aluminium and composite materials are widely used in the automotive industries to produce the adhesively bonded lightweight structures [5]. The mechanical properties of composite materials vary depending on the fiber angle. The behavior of composite single-lap joints under oblique impact load was determined experimentally in the previous study [22]. In the experimental

study, the effects of different impact angles, fiber orientations, and overlap lengths on the impact behavior of adhesively bonded composite single-lap joints were investigated. These parameters affected the composite and adhesive damage characterization. In the experimental study, the determination of the composite damage types and the time-dependent adhesive damage propagation cannot be determined. Determination of composite damage types and time-dependent adhesive damage propagation under impact load in composite joints provides important data for high-strength joint design. Therefore, the development of a realistic numerical model of the composite joints under impact load is important for future academic research and industrial applications [5]. Numerical analysis of composite single-lap joints under impact load allows the determination of adhesive damage initiation and propagation. In addition, it enables the determination of fiber and matrix damage types that occur in composite adherends. In this study, it was aimed to develop a numerical model that could predict the impact behavior and adhesive damage of composite single-lap joints close to the experimental results. The numerical model was validated with the experimental oblique impact results previously determined [22]. The novelty of this study is to determine composite damage types and time-dependent adhesive damage propagation in composite joints under oblique impact load with a realistic numerical model, taking into account different design parameters. Impact analysis of the joints was performed using the three-dimensional explicit finite element method. In the numerical model of the adhesive region, the plastic material behavior of the adhesive was reflected in the analysis by using the elastic–plastic material model, and the adhesive damage initiation and propagation were observed with the CZM. Elastic behavior of composite adherends was defined by the orthotropic material model. In addition, delamination damage and composite damage were determined by cohesive behavior and Hashin’s damage criterion, respectively. The contact force–time diagram, progressive adhesive damage, and composite damage types and distributions are discussed in detail based on the numerical analysis results.

## 2 Experimental Test Details

In a previous study [22], the impact behavior of glass fiber reinforced composite single-lap joints was determined experimentally with the Fractovis Plus impact machine for different impact angles ( $\theta = 0^\circ, 10^\circ, 20^\circ, \text{ and } 30^\circ$ ), fiber angles ( $\phi = 0^\circ, 45^\circ, \text{ and } 90^\circ$ ), and overlap lengths ( $b = 25 \text{ and } 40 \text{ mm}$ ). Glass fiber reinforced composite adherends were produced using the vacuum-assisted resin transfer molding (VARTM) process. Composite single-lap joints were produced with epoxy-based Araldite<sup>®</sup> 2015 adhesive. Impact tests were carried out with an impactor having a radius of 5 mm, a width of 25 mm, and a total mass of 5.302 kg for impact energy of  $E = 3.2 \pm 0.16 \text{ J}$ .

## 3 Finite Element Model

Three-dimensional damage analysis of glass-fiber-reinforced composite single-lap joints under low velocity normal and oblique impact was performed using ABAQUS/Explicit software. The effects of impact angle, fiber angle, and overlap length on the damage initiation and propagation of adhesive in the joint were investigated. In numerical analysis, damage analyses were performed for four different impact angles ( $\theta = 0^\circ, 10^\circ, 20^\circ, \text{ and } 30^\circ$ ), three different fiber angles ( $\phi = 0^\circ, 45^\circ, \text{ and } 90^\circ$ ), and two different overlap lengths ( $b = 25 \text{ and}$

40 mm) at  $E = 3.2$  J impact energy. The deformations that occurred in the impactor during the impact test were negligible. Therefore, the impactor with semi-cylindrical geometry, 5 mm radius, and 25 mm width was modeled as Discrete Rigid. The mass, boundary conditions, and velocity of the impactor were defined at a reference point placed in the center of the impactor. A total mass of 5.302 kg and a velocity of 1.1 m/s were defined to a reference point of the impactor. Only vertical movement ( $y$ -axis) of the impactor was allowed, translational movement in the other two directions ( $x$  and  $z$ -axis), and rotational movement in three axes ( $x, y, z$ ) were prevented (Fig. 1).

The impactor and holders were modeled with R3D4 (4-node 3-D bilinear rigid quadrilateral) and C3D8R (8-node linear brick) element types, respectively. Single-lap joints were positioned between the upper and lower holders. While the movement of the bottom holding apparatus in three axes, as  $x, y,$  and  $z,$  was prevented, the movement of the top holding apparatus was allowed only along the vertical  $y$ -axis to apply pressure to the joint (Fig. 1). The holding pressure has an effect on the stiffness of the joint under bending impact load and affects the contact force variation. In all impact tests, the pressure value provided by the compressor was constant and evenly distributed to the apparatus columns. The holding pressure was calculated by considering the holding force applied to each apparatus and the contact area between the holding apparatus and the joint. As the impact angle increases, the pressure value applied to the holding surface decreases. Therefore, the holding pressure values for each impact angle were calculated approximately by the Statics' equilibrium equations, and these holding pressure values were tested with preliminary numerical analyses. Considering the preliminary numerical analyses to determine the holding pressure value, 16, 8, 4, and 4 bar pressure values were applied to the top holding surface of the single-lap joints for  $0^\circ, 10^\circ, 20^\circ,$  and  $30^\circ$  impact angles, respectively. A general contact algorithm was used in the numerical analysis. Normal and tangential contact behaviors are available in ABAQUS. Under the oblique impact load, the contact area between the impactor and the composite joint increases, and the frictional effects become more effective on the analysis result. Finally, tangential contact behavior was defined for all numerical analyses in order to accurately determine the effect of the oblique impact load on the mechanical behavior of the composite joints. It was determined from the studies in the literature that the friction coefficient between the metal impactor and the composite material was applied

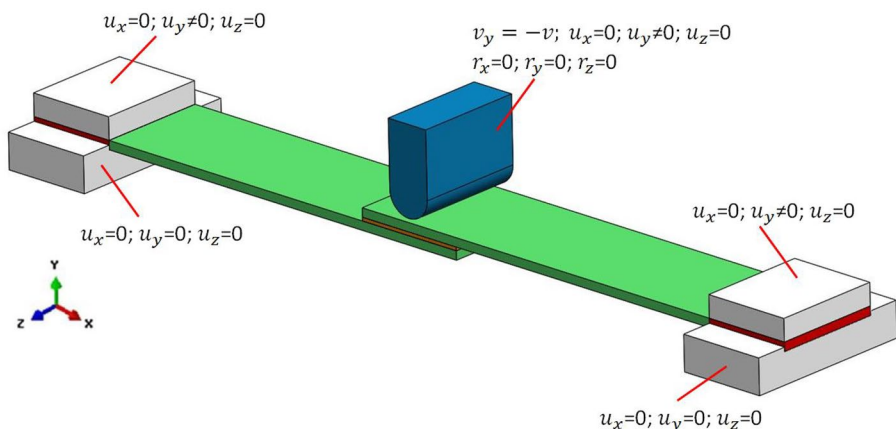


**Fig. 1** Boundary conditions of single-lap joint

as 0.3 in the low-speed impact analysis of the laminated composite structures [23, 24]. For this reason, a friction coefficient of 0.3 was defined between the contacting surfaces of the composite joints with the impactor and holding apparatus.

The finite element modeling of composite materials, adhesive, and interface definitions are explained in Fig. 2. Each ply of composite materials, consisting of four plies, was created separately and combined with the TIE command. The material properties defined for composite adherends are presented in Table 1. Cohesive behavior between the composite plies was defined to determine the delamination between plies. The composite material consists of a resin dense region between each layer. Zhang et al. [24] stated that the interlayer cohesive parameters could not be determined experimentally in their study and they determined the interlayer cohesive parameters using the properties of the matrix material ( $K_n = E_2$ ,  $K_s = K_t = G_{12}$ ,  $t_n^o = Y^T$ ,  $t_s^o = t_t^o = S_{12}$ ,  $G_{IC} = G_{IIC} = G_{III}^c = C_{mt}^c$ ). Using a similar approach, the mechanical properties of epoxy material were used in the interfacial cohesive parameters of the composite plies and the parameters used in the interfacial region are shown in Table 2.

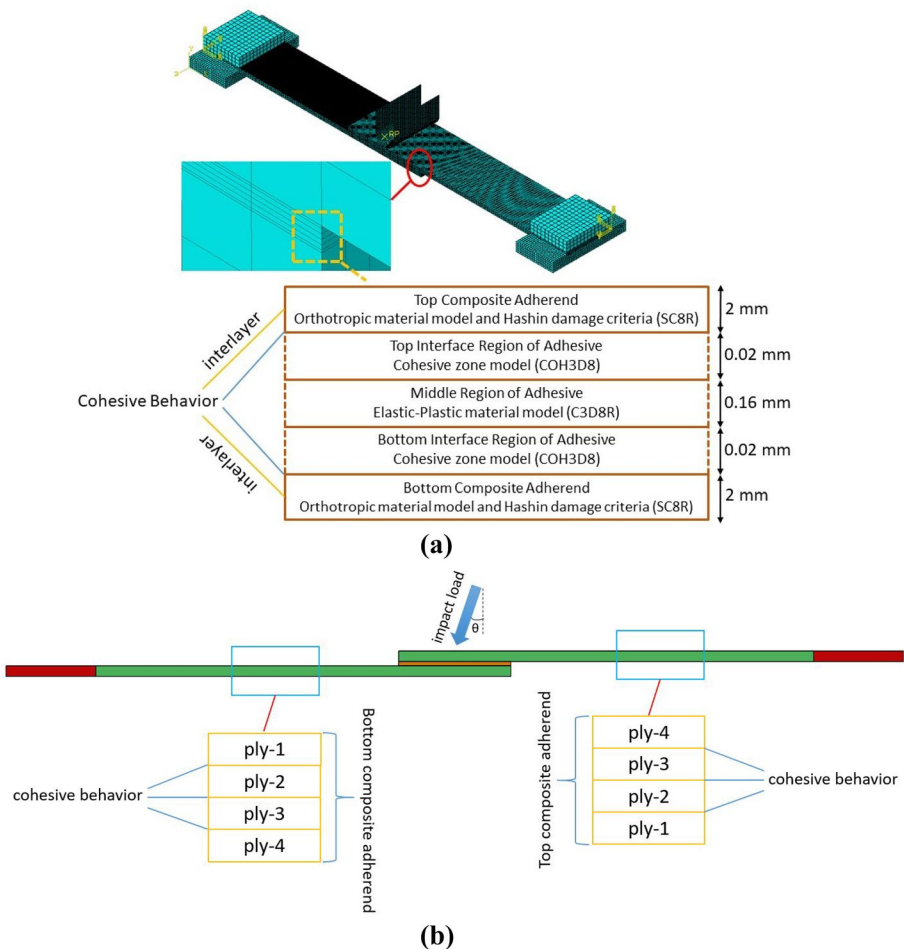


Fig. 2 a Numerical model of single-lap joint, b layer alignment of composite adherends

**Table 1** Mechanical properties of composite material [22]

Property	Symbol	Unit	Value
Longitudinal modulus of elasticity	$E_1$	GPa	34.10
Transverse modulus of elasticity	$E_2 = E_3$	GPa	10.30
Shear modulus	$G_{12} = G_{13}$	GPa	3.60
Shear modulus	$G_{23}$	GPa	3.68
Poisson’s ratio [35]	$\nu_{12} = \nu_{13}$		0.278
Poisson’s ratio [35]	$\nu_{23}$		0.40
Density	$\rho$	kg/m <sup>3</sup>	1830
Longitudinal tensile strength	$X^T$	MPa	750.50
Transverse tensile strength	$Y^T$	MPa	62.80
Longitudinal compressive strength	$X^C$	MPa	248.04
Transverse compressive strength	$Y^C$	MPa	112.40
In-plane shear strength	$S_{12} = S_{13}$	MPa	52.90
Interlaminar shear strength [36, 37]	$S_{23}$	MPa	38
Longitudinal tensile fracture energy [38]	$G_{ft}^c$	N/m	12500
Longitudinal compressive fracture energy [38]	$G_{fc}^c$	N/m	12500
Transverse tensile fracture energy [38]	$G_{mt}^c$	N/m	1000
Transverse compressive fracture energy [38]	$G_{mc}^c$	N/m	1000

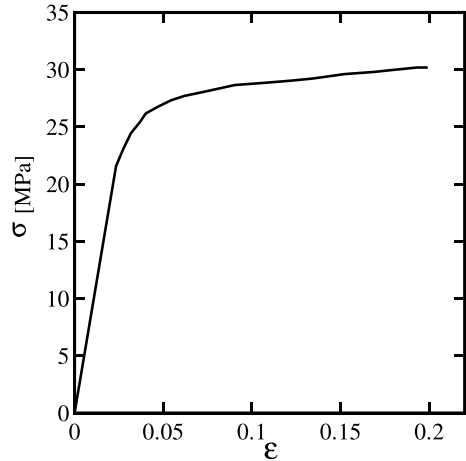
The sequence of the composite plies is shown in Fig. 2. The top and bottom composite adherends of the single-lap joint were defined as Continuum Shell and the mesh structure was created with the SC8R (8-node quadrilateral in-plane general-purpose continuum shell) element type. The finite element model of the adhesive was generated by considering the adhesive damage types in the impact tests. Adhesive damage may show initiation and propagation along the interface, as well as initiation and propagation within the adhesive. The CZM is based on elastic material behavior. Since the adhesive used in the study has a ductile behavior, the behavior of the non-linear plastic material properties should be reflected in the analysis as well as the elastic material behavior of the adhesive. The numerical model of the adhesive consists of three parts (Fig. 2): The top and bottom adhesive interfaces in contact with the composite adherends were modeled using cohesive elements with an artificial thickness value of 0.02 mm. The adhesive region of 0.16 mm thickness between the top and bottom adhesive interfaces was modeled with an elastic–plastic material model using the stress–strain data of Araldite® 2015 adhesive [25]. The stress–strain curve ( $\sigma$ – $\epsilon$ ) of Araldite® 2015 adhesive is shown in Fig. 3 [26]. In order to determine the adhesive damage propagation along the adhesive thickness, the adhesive middle region with a thickness of 0.16 mm was divided into four elements along the thickness. The top and bottom interfaces of the adhesive were modeled with COH3D8 (8-node three-dimensional cohesive element), and the middle region is modeled with C3D8R (8-node linear brick) element type. Mesh intensity is important in terms of solution accuracy. The intensive mesh structure improves the analysis results. However,

**Table 2** Cohesive parameters of composite material [22]

$E$	$G$	$\rho$	$t_n^o$	$t_s^o$	$t_t^o$	$G^c$ [38]
10.3 GPa	3.6 GPa	1190 kg/m <sup>3</sup>	62.8 MPa	52.9 MPa	52.9 MPa	1000 J/m <sup>2</sup>



**Fig. 3** Stress–strain ( $\sigma$ - $\epsilon$ ) curve of Araldite® 2015 adhesive [26]



mesh-intensive analysis increases the solution time. For this reason, with the BIAS command, the mesh element distribution was adjusted with increasing intensity from the ends of the joint to the overlap region.

The composite adherends were modeled as an elastic orthotropic material. Damage types of composite adherends were determined by Hashin’s damage criterion. The parameters of the stiffness matrix in the orthotropic material model also include the elastic constants of the composite material throughout the thickness. In this way, the elastic behavior of the composite material throughout the thickness could be reflected in the analysis. The orthotropic material model and damage estimation in ABAQUS® [27] are performed with formulations developed by Matzenmiller et al. [28], Hashin and Rotem [29], Hashin [30], and Camanho and Davila [31]. Stress–strain ( $\sigma$ - $\epsilon$ ) relations of linear elastic material behavior of orthotropic material are as follows in matrix form.

$$\begin{bmatrix} \sigma_{11} \\ \sigma_{22} \\ \sigma_{33} \\ \sigma_{12} \\ \sigma_{13} \\ \sigma_{23} \end{bmatrix} = \begin{bmatrix} D_{1111} & D_{1122} & D_{1133} & 0 & 0 & 0 \\ & D_{2222} & D_{2233} & 0 & 0 & 0 \\ & & D_{3333} & 0 & 0 & 0 \\ & & & D_{1212} & 0 & 0 \\ & & & & D_{1313} & 0 \\ & & & & & D_{2323} \end{bmatrix} \begin{bmatrix} \epsilon_{11} \\ \epsilon_{22} \\ \epsilon_{33} \\ \gamma_{12} \\ \gamma_{13} \\ \gamma_{23} \end{bmatrix} \tag{1}$$

$$\begin{aligned}
 D_{1111} &= E_1(1 - \nu_{23}\nu_{32})\Delta \\
 D_{2222} &= E_2(1 - \nu_{13}\nu_{31})\Delta \\
 D_{3333} &= E_3(1 - \nu_{12}\nu_{21})\Delta \\
 D_{1122} &= E_1(\nu_{21} + \nu_{31}\nu_{23})\Delta = E_2(\nu_{12} + \nu_{32}\nu_{13})\Delta \\
 D_{1133} &= E_1(\nu_{31} + \nu_{21}\nu_{32})\Delta = E_3(\nu_{13} + \nu_{12}\nu_{23})\Delta \\
 D_{2233} &= E_2(\nu_{32} + \nu_{12}\nu_{31})\Delta = E_3(\nu_{23} + \nu_{21}\nu_{13})\Delta \\
 D_{1212} &= G_{12} \\
 D_{1313} &= G_{13} \\
 D_{2323} &= G_{23}
 \end{aligned} \tag{2}$$

$$\Delta = \frac{1}{1 - \nu_{12}\nu_{21} - \nu_{23}\nu_{32} - \nu_{31}\nu_{13} - 2\nu_{21}\nu_{32}\nu_{13}} \tag{3}$$

In ABAQUS® finite element software, damage initiation and propagation of fiber-reinforced composite materials are determined according to Hashin’s [29] damage criterion. Hashin’s damage criterion considers four main damage mechanisms: fiber tensile damage, fiber compression damage, matrix tensile damage, and matrix compression damage [27]. Namely,

Fiber tension ( $\hat{\sigma}_{11} \geq 0$ ):

$$F_f^t = \left( \frac{\hat{\sigma}_{11}}{X^T} \right)^2 + \alpha \left( \frac{\hat{\tau}_{12}}{S^L} \right)^2 \tag{4}$$

Fiber compression ( $\hat{\sigma}_{11} < 0$ ):

$$F_f^c = \left( \frac{\hat{\sigma}_{11}}{X^C} \right)^2 \tag{5}$$

Matrix tension ( $\hat{\sigma}_{22} \geq 0$ ):

$$F_m^t = \left( \frac{\hat{\sigma}_{22}}{Y^T} \right)^2 + \left( \frac{\hat{\tau}_{12}}{S^L} \right)^2 \tag{6}$$

Matrix compression ( $\hat{\sigma}_{22} < 0$ ):

$$F_m^c = \left( \frac{\hat{\sigma}_{22}}{2S^T} \right)^2 + \left[ \left( \frac{Y^C}{2S^T} \right)^2 - 1 \right] \frac{\hat{\sigma}_{22}}{Y^C} + \left( \frac{\hat{\tau}_{12}}{S^L} \right)^2 \tag{7}$$

In the formulas above,  $X^T$ ,  $X^C$ ,  $Y^T$ ,  $Y^C$ ,  $S^L$ , and  $S^T$  indicate longitudinal tensile strength, longitudinal compressive strength, transverse tensile strength, transverse compressive strength, longitudinal shear strength, and transverse shear strength, respectively.

Campilho et al. [32] determined the cohesive parameters of Araldite® 2015 adhesive. In the adhesive numerical model, the top and bottom cohesive interfaces were modeled using these parameters. The maximum nominal stress criterion was used for determining the damage initiation, and damage propagation was determined using the failure displacement value of Araldite® 2015 adhesive with linear damage evolution criteria. In the maximum nominal stress criterion, cohesive damage initiates when any of the traction ratios in the normal and two shear directions reach one value as follows [27].

$$\max \left\{ \frac{\langle t_n \rangle}{t_n^o}, \frac{t_s}{t_s^o}, \frac{t_t}{t_t^o} \right\} = 1 \tag{8}$$

where  $\langle \rangle$  is Macaulay bracket symbol,  $t_n^o$ ,  $t_s^o$ , and  $t_t^o$  represent normal and shear tractions depending on the material strength, respectively. Depending on the cohesive damage condition, the traction values vary according to the expressions below [27].

$$t_n = (1 - D)\bar{t}_n, \quad \text{if } \bar{t}_n \geq 0 \tag{9}$$

$$t_n = \bar{t}_n, \quad \text{if } \bar{t}_n < 0 \text{ (no damage)} \tag{10}$$

$$t_s = (1 - D)\bar{t}_s \tag{11}$$

$$t_t = (1 - D)\bar{t}_t \tag{12}$$

where  $\bar{t}_n$ ,  $\bar{t}_s$ , and  $\bar{t}_t$  are the stress components in case the damage has not yet formed. The effective interfacial separation ( $\delta_m$ ) can be written as follows depending on the interfacial separation values in the normal ( $\delta_n$ ) and two shear directions ( $\delta_s$  and  $\delta_t$ ).

$$\delta_m = \sqrt{\langle \delta_n \rangle^2 + \delta_s^2 + \delta_t^2} \tag{13}$$

The damage parameter  $D$  can be expressed in linear and exponential form and is used to predict damage evolution. The linear damage evolution criterion can be expressed as follows.

$$D = \frac{\delta_m^f (\delta_m^{max} - \delta_m^o)}{\delta_m^{max} (\delta_m^f - \delta_m^o)} \tag{14}$$

and the exponential damage evolution criterion can be expressed as follows.

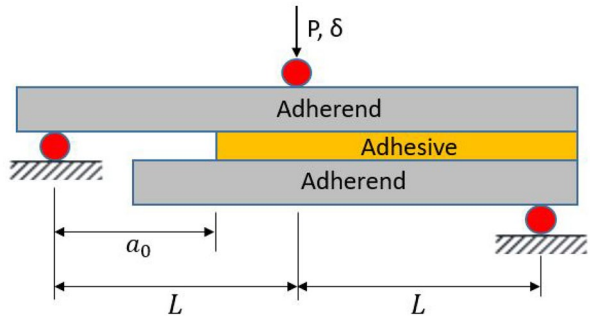
$$D = 1 - \left\{ \frac{\delta_m^o}{\delta_m^{max}} \right\} \left\{ 1 - \frac{1 - \exp(-\alpha(\frac{\delta_m^{max} - \delta_m^o}{\delta_m^f - \delta_m^o}))}{1 - \exp(-\alpha)} \right\} \tag{15}$$

$\delta_m^o$ ,  $\delta_m^f$  and  $\delta_m^{max}$  are called as effective interfacial separation at failure initiation, effective interfacial separation at failure, and effective interfacial separation at complete failure, respectively [27, 31].  $\alpha$  represents a non-dimensional damage parameter.

Experimental geometric condition of adhesively bonded single-lap joints under bending impact load is similar to the MMF (Mixed-mode flexure) test. The schematic representation of the MMF test is presented in Fig. 4 [33]. In the MMF test, the adhesively bonded specimen is exposed to peeling and shear stresses under three-point bending load. In this way, the mixed-mode fracture behavior of the adhesive joints is determined with MMF test. The mixed mode fracture energy and failure displacement values obtained from the MMF test are used to determine the damage evolution in the adhesive numerical model. Wong [34] measured the failure displacement value of the Araldite® 2015 adhesive as 0.065 mm in the MMF test. Damage propagation in the cohesive region was determined using this value (0.065 mm). The mechanical and cohesive properties used in the numerical model of adhesive are presented in Table 3 [32, 34].

The damage initiation in the elastic–plastic adhesive region with a thickness of 0.16 mm between the top and bottom cohesive interfaces of the adhesive was determined using failure strain ( $\epsilon_f = 0.17$ ). The failure strain value was obtained from the stress–strain curve [26]. The damage propagation in this region was determined using the failure displacement value ( $\delta^f = 0.065$  mm) obtained from the MMF test of the adhesive. Cohesive behavior was defined between the surfaces of the adhesive in contact with the composite adherends. In this way, possible numerical errors due to sudden changes in mechanical properties were prevented (Fig. 2).

**Fig. 4** Schematic representation of the mixed mode flexure (single-leg bending) test condition



### 4 Comparison of Numerical and Experimental Results

Finite element analysis allows determination of the effects of various parameters on mechanical behavior and monitoring damage occurrences in terms of engineering applications. Transforming the mechanical behavior of materials determined by experimental methods into a suitable mathematical model and adapting them to the finite element method provides material, time, and cost savings. In order to evaluate the numerical model of adhesively bonded composite single-lap joints, contact force-time, composite adherend damage, and adhesive damage were investigated and compared with the experimental results.

#### 4.1 Comparison of Contact Force-Time Graphs

The low-velocity impact behavior of glass fiber reinforced composite joints with different impact angles ( $\theta = 0^\circ, 10^\circ, 20^\circ$  and  $30^\circ$ ), fiber angles ( $\phi = 0^\circ, 45^\circ$ , and  $90^\circ$ ), and overlap lengths ( $b = 25$  and  $40$  mm) were investigated numerically. The contact force-time variation obtained from finite element analysis was compared with the experimental ones. Contact force-time variation provides important data such as the load-carrying capacity of the joint under dynamic load and the determination of damage evaluation stages. The maximum contact force that occurs in the joint under impact load provides information about the bending strength of the joint, while the total contact time provides information about the elastic deformation capacity of the joint.

The experimental and numerical contact force-time variations of glass fiber reinforced composite single-lap joints with  $0^\circ$  fiber angle for different impact angles and overlap lengths are shown in Fig. 5. There is generally good agreement between the experimental and numerical contact force-time variations for all impact angles and overlap lengths. While the increase in the impact angle maintained the agreement between the experimental and numerical values of the maximum contact force occurring in the joints, the same agreement was not observed between the total contact time values. For high impact angles ( $20^\circ$  and  $30^\circ$ ), after the impact load was applied to the joint, the remaining energy was very small levels, so the anti-rebound system of the impact device could not hold the impactor.

**Table 3** Mechanical and cohesive parameters of Araldite® 2015 adhesive [32, 34]

$E$	$G$	$\nu$	$t_n^\circ$	$t_s^\circ$	$t_t^\circ$	$\rho$	$\delta_f(MMF)$
GPa	GPa		MPa	MPa	MPa	kg/m <sup>3</sup>	mm
1.85	0.56	0.33	21.63	17.9	17.9	1400	0.065

Impact angle

$b = 25 \text{ mm}$

$b = 40 \text{ mm}$

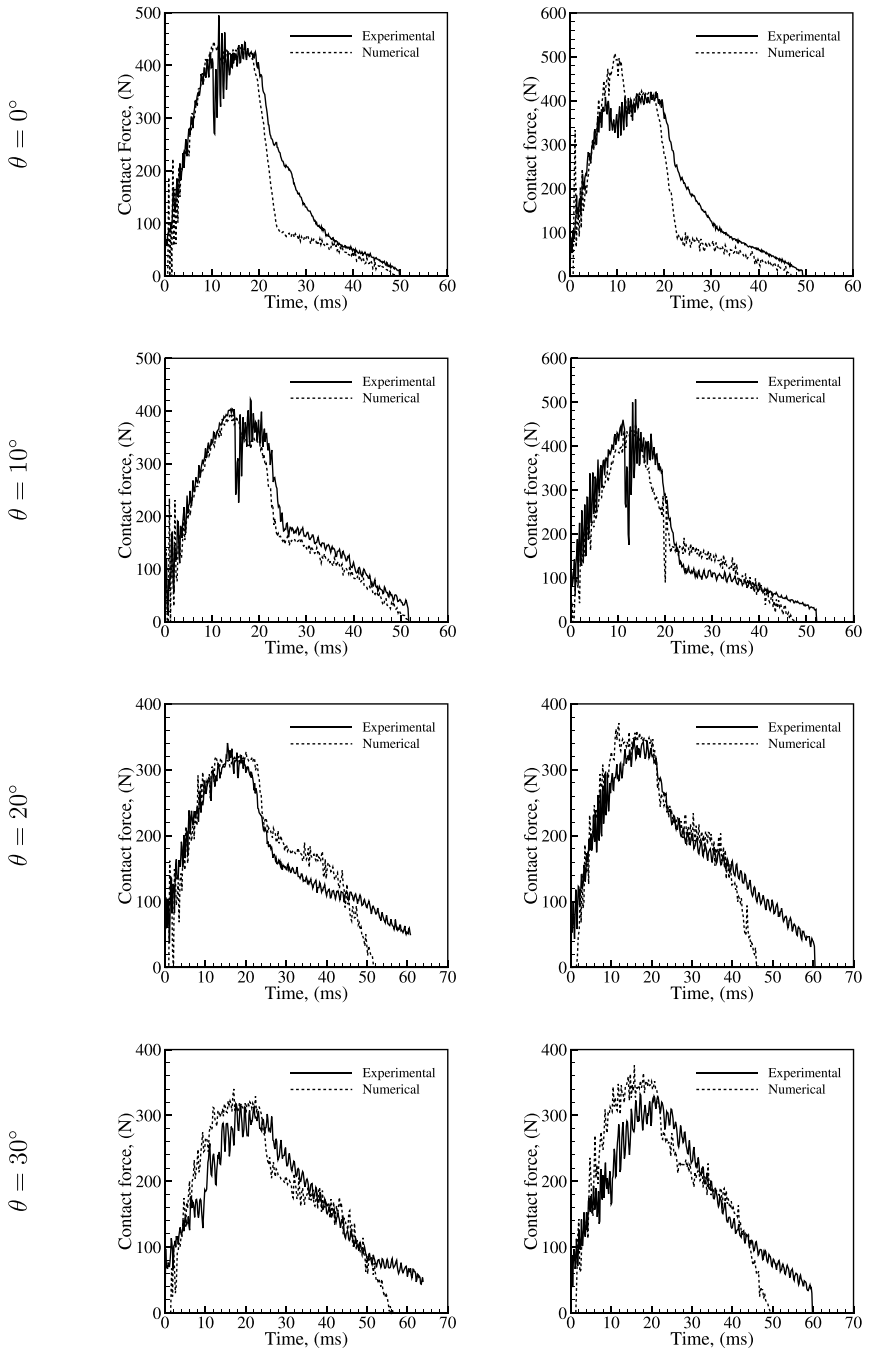


**Fig. 5** Comparison of experimental and numerical contact force-time variations of composite single-lap joints with  $0^\circ$  fiber angle ( $b$ : overlap length,  $\theta$ : impact angle)

As a result of this, the contact between the impactor and the joint continued, and the contact force value could not reach zero value. However, this situation did not happen in the numerical analysis. Therefore, as the impact angle increased, the difference between the experimental and numerical total contact time values showed a partial increase.

Since the adhesively bonded composite joint with  $45^\circ$  fiber angle has an unsymmetrical structure, it is forced to rotate around its longitudinal axis under bending impact load. This situation was observed in both impact tests and numerical analysis. The experimental and numerical contact force-time variations of the composite joints with  $45^\circ$  fiber angle are compared in Fig. 6. Experimental and numerical maximum contact force and total contact time values for  $0^\circ$  and  $10^\circ$  impact angles showed good agreement. With the increase in the impact angle, the difference between the experimental and numerical maximum contact force and the total contact time slightly increased. Composite joints release the elastic deformation energy gained by the impact load after the contact force reaches the maximum value. For high impact angles ( $20^\circ$  and  $30^\circ$ ), the experimental contact force value could not reach zero since the contact between the impactor and the joint continued during the release of elastic energy. In the numerical analysis, however, the contact force value reached zero after the joint completely released the elastic energy. The difference between the experimental and numerical total contact time values was greatest in the joint with  $45^\circ$  fiber angle and  $30^\circ$  impact angle. There is a good agreement between the experimental and numerical results up to the highest level of contact force during impact loading. However, after this point, the rebound stage begins, and since the contact between the joint and the impactor was not interrupted for a longer period of time during the impact test, small differences occurred between the experimental and numerical variations. In addition, the difference between the experimental and numerical results was relatively higher in the joint with  $45^\circ$  fiber angle, which was related to the damage model. In order to reflect the mechanical properties of the composite material in three directions in the numerical model, the elastic behavior of the composite material was applied by using the orthotropic material model. However, the damage was determined by taking into account the plane stress state. A cohesive surface was defined between each composite ply to observe the delamination while ignoring the damage assessment along the thickness direction of each composite ply. The orthotropic material model provided a close estimation of the impact behavior since no significant damage occurred in the composite adherends for the joint with  $0^\circ$  fiber angle. The impact load was carried by the fiber and matrix region for the joint with  $45^\circ$  fiber angle. For this reason, it caused the fiber-matrix interface region to be forced by the impact load and damage occurred along the thickness direction of the composite material. In addition, the effect of shear stress on damage became more evident in these joints. As a result, the numerical model estimated the maximum contact force higher than the experimental results because it neglected the damage along the thickness direction of each composite ply.

The contact force-time variations of joints with  $90^\circ$  fiber angle are compared in Fig. 7. There is a good agreement between the experimental and numerical results for the joints with  $90^\circ$  fiber angle. The joint with  $90^\circ$  fiber angle is the joint with the weakest bending stiffness. Since the fibers are positioned parallel to the loading line, the bending impact load causes high axial normal stresses, the fibers placed in this direction carry these stresses together with the matrix material. A small amount of adhesive damage and matrix shear damage were observed in the joints with  $90^\circ$  fiber angle. The contact force-time variations exhibited significant oscillations due to local damage in the composite plies and the adhesive. While the maximum contact force value decreased with the increase in the impact angle, the total contact time increased. There is a good agreement between the

Impact angle

$b = 25$  mm

$b = 40$  mm

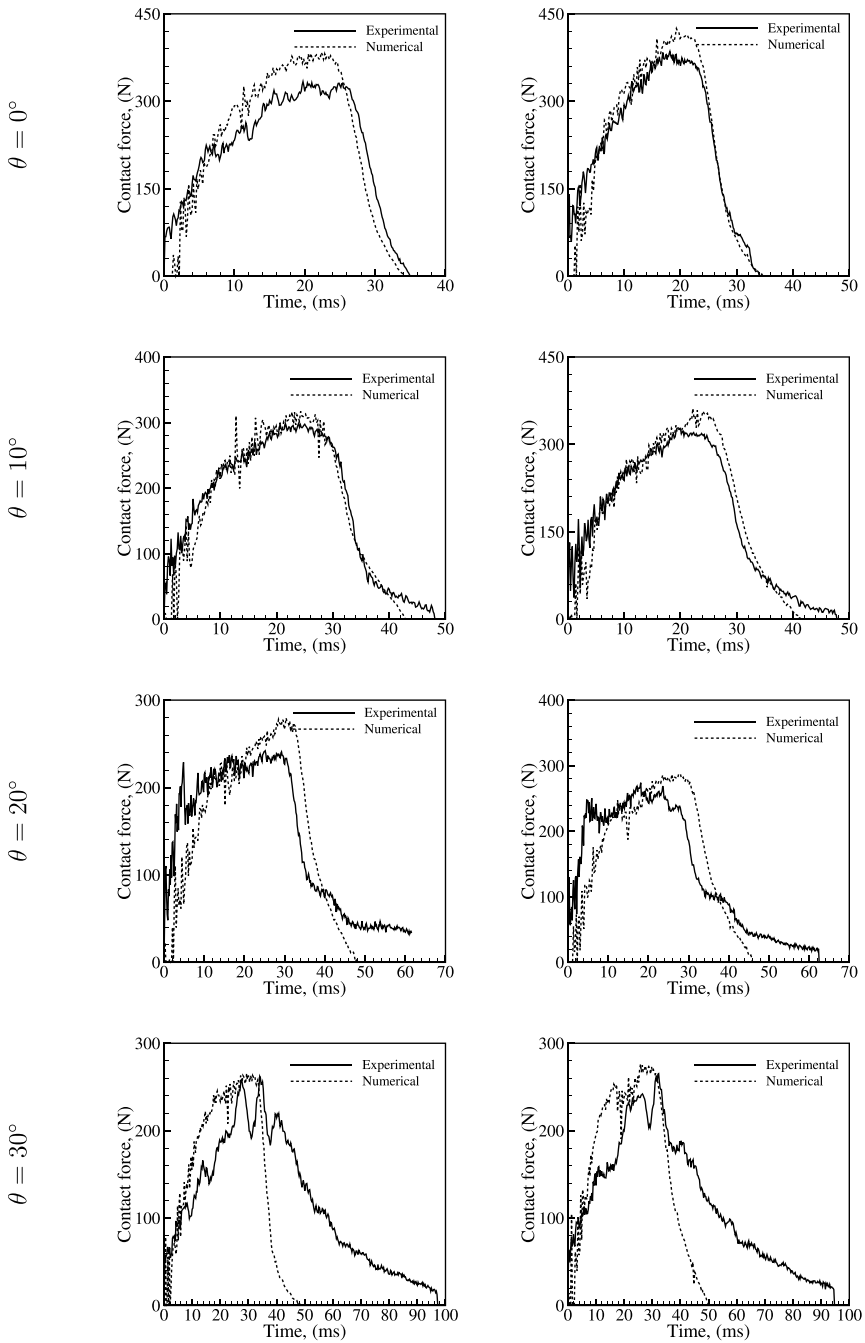


**Fig. 6** Comparison of experimental and numerical contact force-time variations of composite single-lap joints with 45° fiber angle ( $b$ : overlap length,  $\theta$ : impact angle)

Impact angle

$b = 25$  mm

$b = 40$  mm

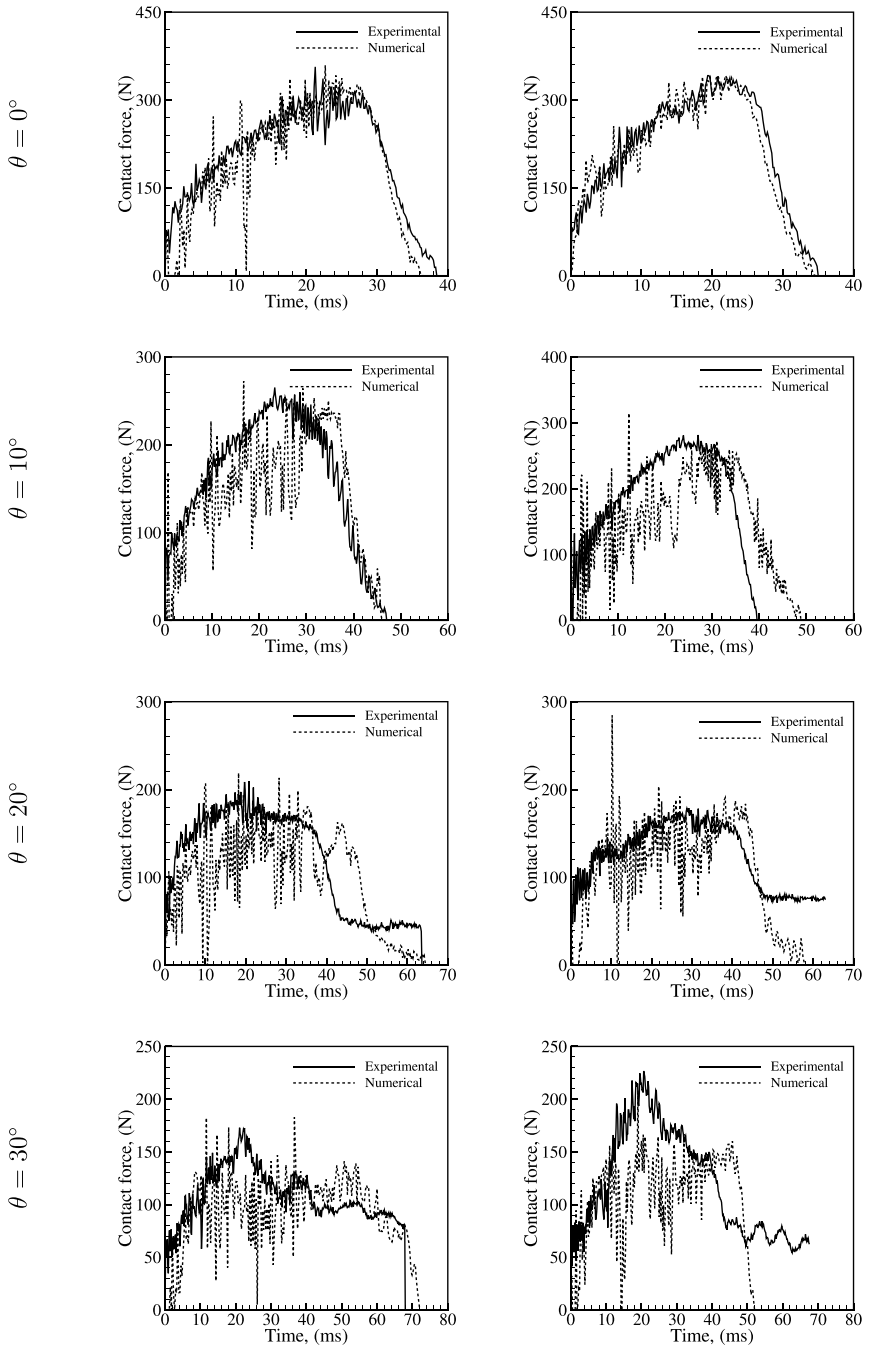


**Fig. 7** Comparison of experimental and numerical contact force-time variations of composite single-lap joints with  $90^\circ$  fiber angle ( $b$ : overlap length,  $\theta$ : impact angle)



experimental and numerical results for  $0^\circ$  and  $10^\circ$  impact angles. While this agreement was maintained for the contact force at high impact angles ( $20^\circ$  and  $30^\circ$ ), it differed negligibly for the total contact time.

The orientation of the fiber angles determines the bending stiffness of the joint. In the joints with  $0^\circ$  fiber angle having the highest bending stiffness, the bending impact load was carried by the fibers and the adhesive. Since the bending strength of the fibers is higher than the adhesive peel strength, the applied impact energy caused a large amount of adhesive damage. Some of the applied impact energy caused adhesive damage and, the remaining energy was stored as elastic strain energy, causing the impactor to rebound. The contact force-time variations showed that as the flexural stiffness of the joint increased, the loading time became shorter than the rebound time. Namely, as the amount of damage in composite adherends and adhesive increased, a large part of the applied impact energy caused these damage and the loading time increased. Increasing the fiber angle decreased the amount of impact load carried by the fibers and increased in-plane shear stresses in the fiber-matrix interface. Increased shear stresses caused composite damage for the joints with  $45^\circ$  and  $90^\circ$  fiber angles. The difference between numerical and experimental maximum contact force values for the joints with 25 mm overlap length is 4–11%, 1–15%, and 1–6% for  $0^\circ$ ,  $45^\circ$ , and  $90^\circ$  fiber angles, respectively, while this difference for the joints with 40 mm overlap length is 7–21%, 4–10%, and 1–12% for  $0^\circ$ ,  $45^\circ$ , and  $90^\circ$  fiber angles, respectively. In addition, the difference between numerical and experimental total contact time values for the joints with 25 mm overlap length is 1–16%, 2–28%, and 1–6% for  $0^\circ$ ,  $45^\circ$ , and  $90^\circ$  fiber angles, respectively, while this difference for the joints with 40 mm overlap length is 4–30%, 2–27%, and 1–30% for  $0^\circ$ ,  $45^\circ$ , and  $90^\circ$  fiber angles, respectively. Percentage values were determined according to the smallest and largest values for different impact angles.

## 4.2 Comparison of Adhesive Damage

The types of damage initiation and propagation regions provide important information for determining the mechanical behavior of adhesively bonded composite single-lap joints under oblique impact. Adhesive damage was determined according to the SDEG (Scalar Stiffness Degradation Variable) damage parameter. SDEG value varied between 0 and 1. A value of 1 indicates a completely damaged element, while a value of 0 indicates an undamaged element. In numerical analysis, adhesive damage was determined by removing the elements with SDEG coefficient values of 0.99 and above. The completely damaged adhesive layer is represented by gray and the undamaged part is represented by blue. The experimental and numerical adhesive damage areas in composite single-lap joints with different fiber angles are compared in Fig. 8. The separation length value is written in the gray bar. The fiber angle affected the adhesive damage initiation and propagation mechanism. In the joint with  $0^\circ$  fiber angle, the adhesive damage propagated regularly along the overlap region, while in the joint with  $45^\circ$  fiber angle, the adhesive damage propagated along the fiber angle direction. After the impact test, the damaged surfaces were photographed with a LED light source in a dark room. Damaged areas were darker than non-damaged areas. Thanks to this color tone difference, experimental adhesive damage lengths and areas could be determined. For the joints with  $0^\circ$  fiber angle, adhesive damage areas in the joints having  $0^\circ$  and  $10^\circ$  impact angles were greater than the joints having  $20^\circ$  and  $30^\circ$  impact angles. There was a small amount of adhesive damage that could not be detected by the imaging method for  $20^\circ$  and  $30^\circ$  impact angles. With the effect of increasing shear stresses in these joints, the adhesive damage turned into the matrix shear damage and the damage progressed in the matrix region. A similar pattern of damage

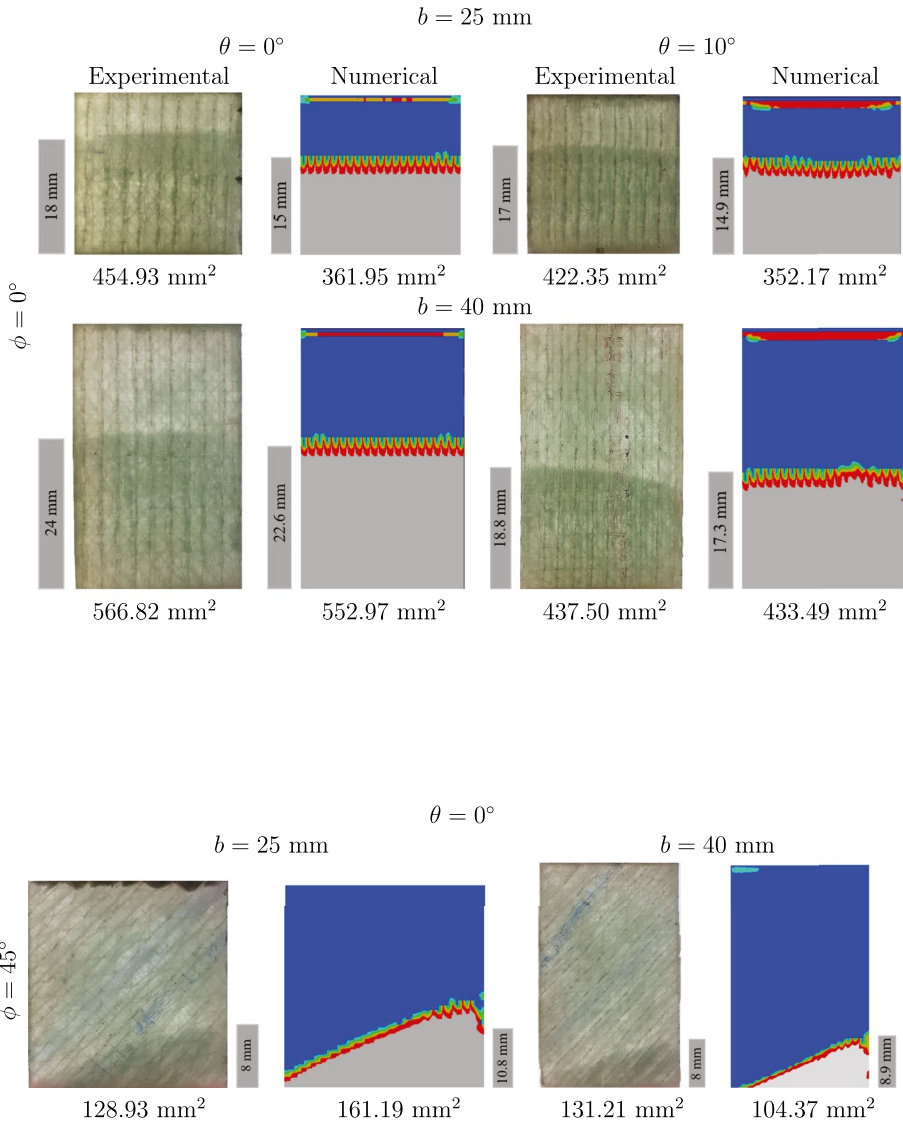


**Fig. 8** Experimental and numerical adhesive damage areas in composite single-lap joints ( $\phi$ : fiber angle,  $\theta$ : impact angle,  $b$ : overlap length)

occurred in the joints with  $90^\circ$  fiber angle. Therefore, the damage surfaces for the joints having  $0^\circ$  and  $10^\circ$  impact angles,  $0^\circ$  fiber angle, and 25 and 40 mm overlap lengths were investigated in detail, experimentally and numerically.

While the adhesive damage for the joints having  $0^\circ$  impact angle and  $45^\circ$  fiber angle can be observed, the images did not provide qualified information since very little adhesive damage occurred in the joints having  $10^\circ$ ,  $20^\circ$ , and  $30^\circ$  impact angles. There is a good agreement between numerical and experimental adhesive damage areas in the joints with  $0^\circ$  and  $10^\circ$  impact angles, and  $0^\circ$  fiber angle. Experimental and numerical adhesive damage for both

joints progressed smoothly, initiating from the right free edge of the overlap towards the middle region. (E)xperimental and (N)umerical adhesive damage area ratios were compared for 25 and 40 mm overlap lengths. The total overlap areas were 625 and 1000 mm<sup>2</sup> for 25 and 40 mm overlap lengths, respectively. In the joint with 0° impact angle and 0° fiber angle, the percentage of the damaged adhesive area to the total overlap area was 73% (E), 58% (N) for 25 mm overlap length and 57% (E), 55% (N) for 40 mm overlap length. The increase in overlap length had a positive effect on the load-carrying capacity of the joint. For the same impact energy, an increase in the overlap length decreased the rate of the damaged adhesive area. For the joints with 10° impact angle, the adhesive damage rate was 68% (E), 56% (N) for 25 mm overlap length, while this rate was 44% (E), 43% (N) for 40 mm overlap length. The ratio of damaged adhesive area decreased with the increase in the impact angle.

The impact energy applied in the joint having 45° fiber angle caused different types of adhesive damage. Adhesive damage rates decreased due to the more pronounced shear effects and wider damage areas in composite adherends. Adhesive damage rates are 21% (E), 26% (N) and 13% (E), 10% (N) for 25 and 40 mm overlap lengths, respectively. Experimental and numerical damage results of the joints with 90° fiber angle showed that a small amount of adhesive damage was accompanied by significant matrix shear damage. The bending strength of the matrix material was weaker than the peel strength of the adhesive. As the bending stiffness of the joints increased, the adhesive damage also increased. For this reason, the adhesive damage was the highest in the joint with 0° fiber angle and the least in the joint with 90° fiber angle. Since very little damage occurred in the composite adherends for the joint with 0° fiber angle under impact load, the impact load (energy) was mostly carried by the adhesive layer and significant adhesive damage occurred. In the joints with 45° and 90° fiber angles, since the impact energy caused composite damage, the impact energy transmitted to the adhesive layer decreased and caused less adhesive damage.

The use of the CZM in the two adhesive interfaces and the elastic–plastic material model between these two interfaces was successful in predicting adhesive damage. Experimental and numerical adhesive damage showed improvement along the fiber direction of the composite adherends.

## 5 Investigation of Time-Dependent Adhesive Damage Initiation and Propagation

The impact load is transferred to the joint in a very short time. Therefore, damage initiates and propagates very quickly. Observing and recording the damage during the test in the experimental study requires costly equipment. It was aimed to develop a numerical model that provides results compatible with the experimental results, and is possible to predict the damage initiation and propagation, which is difficult to detect experimentally. The time-dependent adhesive damage distribution and axial damage propagation ( $\Delta_{(N)umerical}$ ) of the joints with 0° fiber angle and 25 mm overlap length are shown in Fig. 9. Adhesive damage initiated at approximately 5 ms contact time, while the initiation time of damage delayed as the impact angle increased. Adhesive damage propagated smoothly from the side free edges of the adhesive to the middle region for all impact angles. While the increase in the impact angle caused a delay in the adhesive damage initiation, it did not have a significant effect on the distributions of damage propagation. The fiber angle of the composite adherends had a great effect on the distribution of adhesive damage propagation. When the contact force reached the maximum value, the adhesive damage area reached the highest level. In the impactor rebound phase, there was a slight increase in adhesive damage propagation. The experimental and numerical adhesive damage

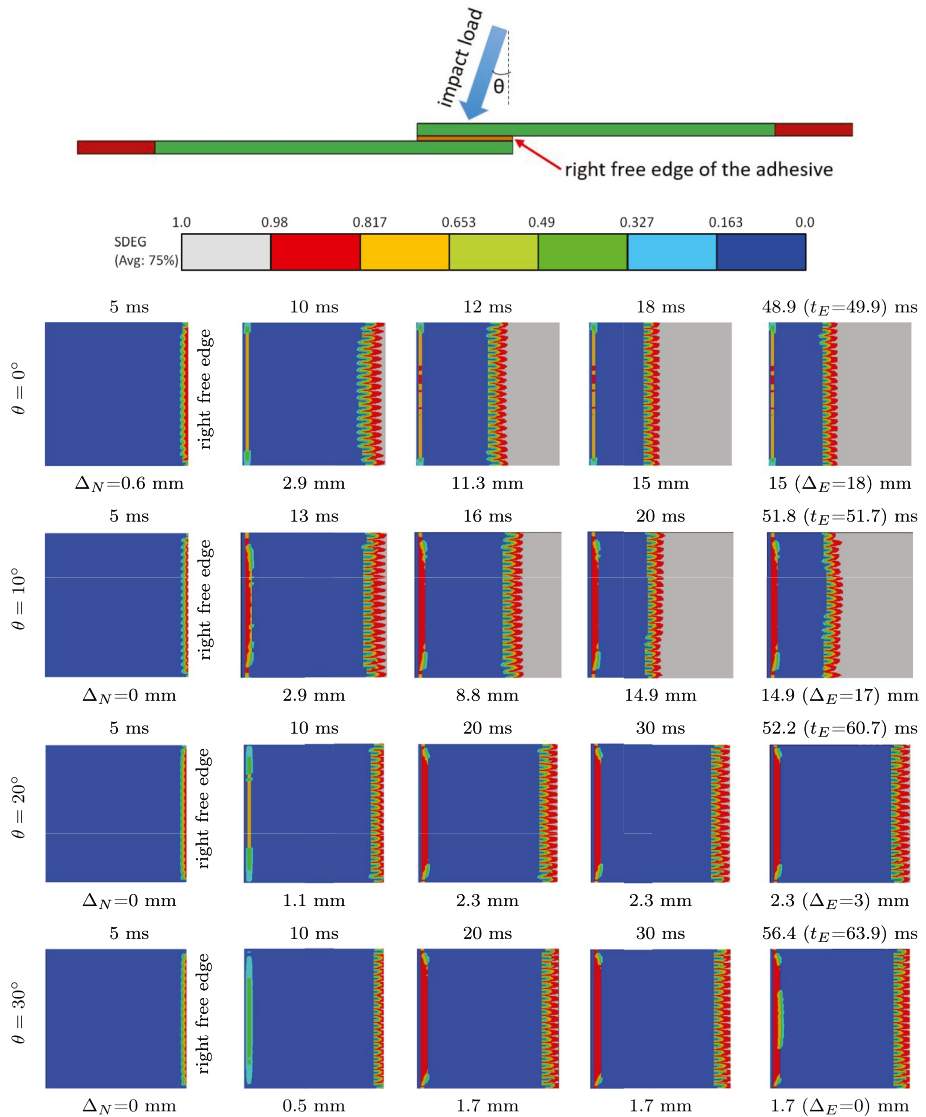


**Fig. 9** Adhesive damage initiation and propagation in joints with  $0^\circ$  fiber angle and 25 mm overlap length ( $\theta$ : impact angle)

areas decreased with the increase in the impact angle. The toughness of Araldite<sup>®</sup> 2015 adhesive in normal and shear directions were determined by Campilho et al [32]. They determined the toughness as 0.43 N/mm in the normal direction and 4.7 N/mm in the shear direction. The toughness of Araldite 2015 adhesive in the shear direction is greater than the toughness in the normal direction. As the impact angle increases, the normal component of the impact load decreases, while the axial and lateral shear components increase. As the shear toughness of Araldite<sup>®</sup> 2015 adhesive was higher than the normal toughness, the damage that occurred in the joint under shear forces decreased with the increase in the impact angle. The increase in impact angle increased the numerical and experimental total contact time.

Adhesive damage distributions for the joints with 45° fiber angle and 25 mm overlap length are shown in Fig. 10. Fiber orientation of composite adherends significantly affected the adhesive damage initiation and propagation. Adhesive damage initiated and propagated in the fiber direction. The increase in the impact angle partially delayed the adhesive damage initiation and affected the adhesive damage distributions. The adhesive numerical model consisted of three different parts (Fig. 2). For the joints with 0° and 45° fiber angles, adhesive damage initiated and propagated along the top adhesive interface. Adhesive damage initiation and propagation of the joints with 90° fiber angle and 25 mm overlap length are shown in Fig. 11. The bending impact load was covered by the matrix and the adhesive for the joints

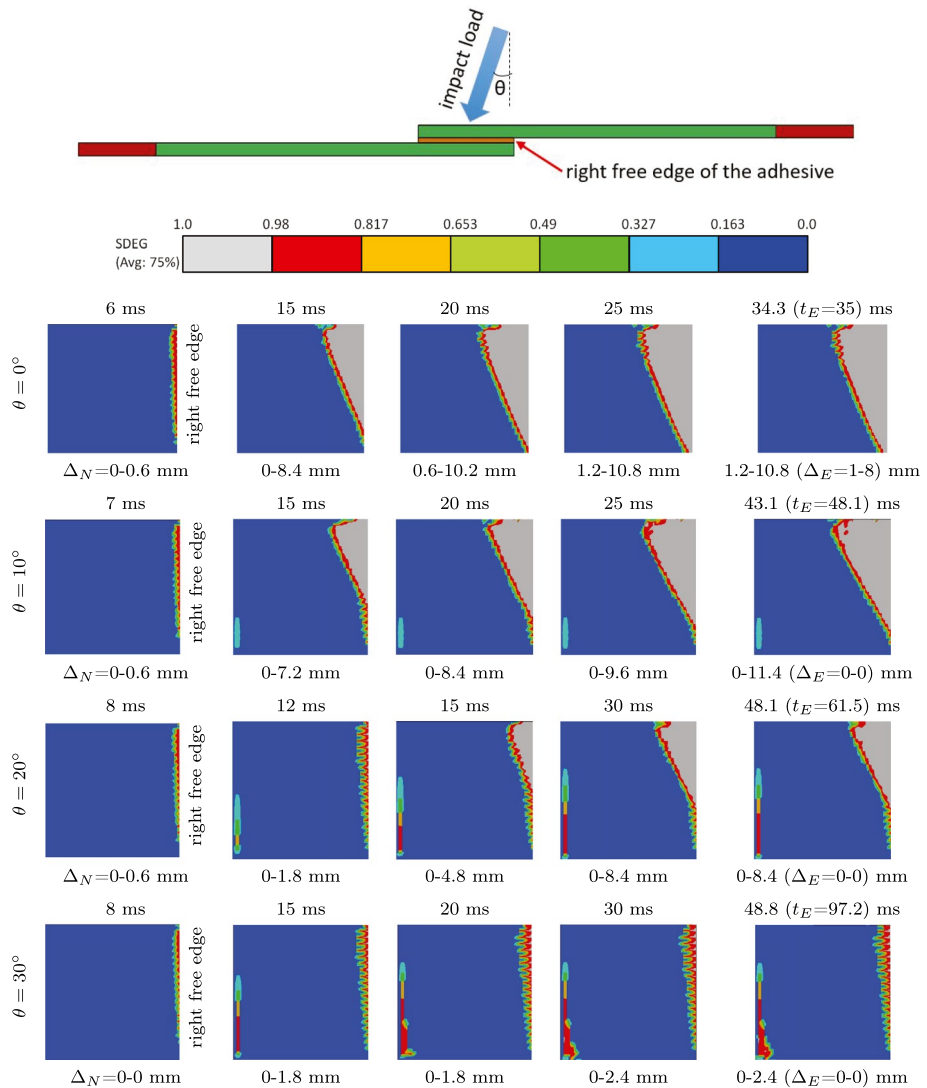


**Fig. 10** Adhesive damage initiation and propagation in joints with 45° fiber angle and 25 mm overlap length ( $\theta$ : impact angle)

with 90° fiber angle. Since the matrix material was exposed to more stress and deformation than the adhesive, matrix shear damage was observed with the effect of shear stresses. A small amount of adhesive damage occurred with matrix shear damage. While the adhesive region was under the effect of peeling stresses for normal impact, shear stress became more effective in adhesive and composite adherends with the increase in impact angle. Increasing shear stresses caused the matrix shear damage and the damage area in the adhesive region decreased. The adhesive showed better strength load under increasing shear stress.

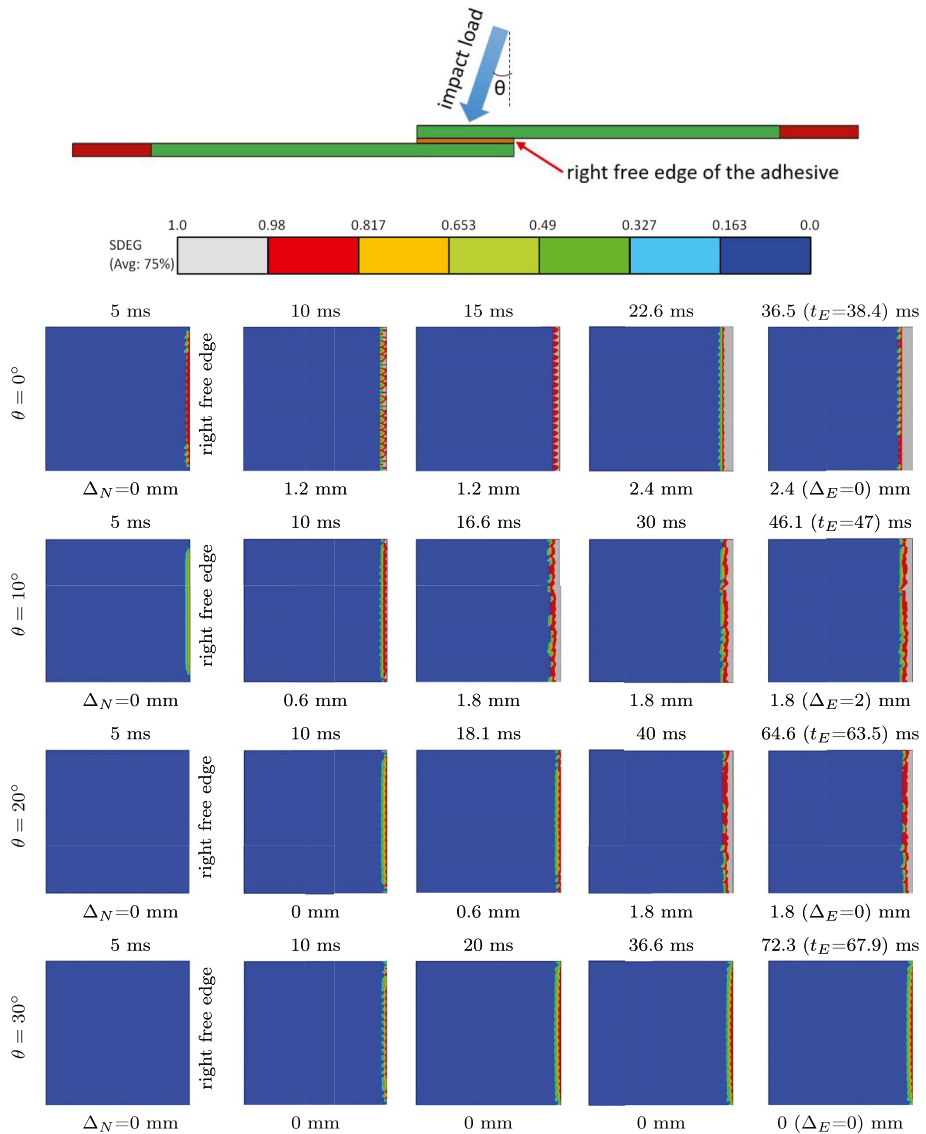


**Fig. 11** Adhesive damage initiation and propagation in joints with 90° fiber angle and 25 mm overlap length ( $\theta$ : impact angle)

Axial separation ( $\Delta_{N'}^{(numerical)}$ )-time variations of composite single-lap joints with different fiber angles are compared in Fig. 12. The experimental separation value is shown in parentheses next to the numerical axial separation value. Adhesive damage initiated and propagated in 0-20 ms time intervals in the joints with 0° fiber angle. The greatest axial separation value occurred at 20 ms and then damage propagation

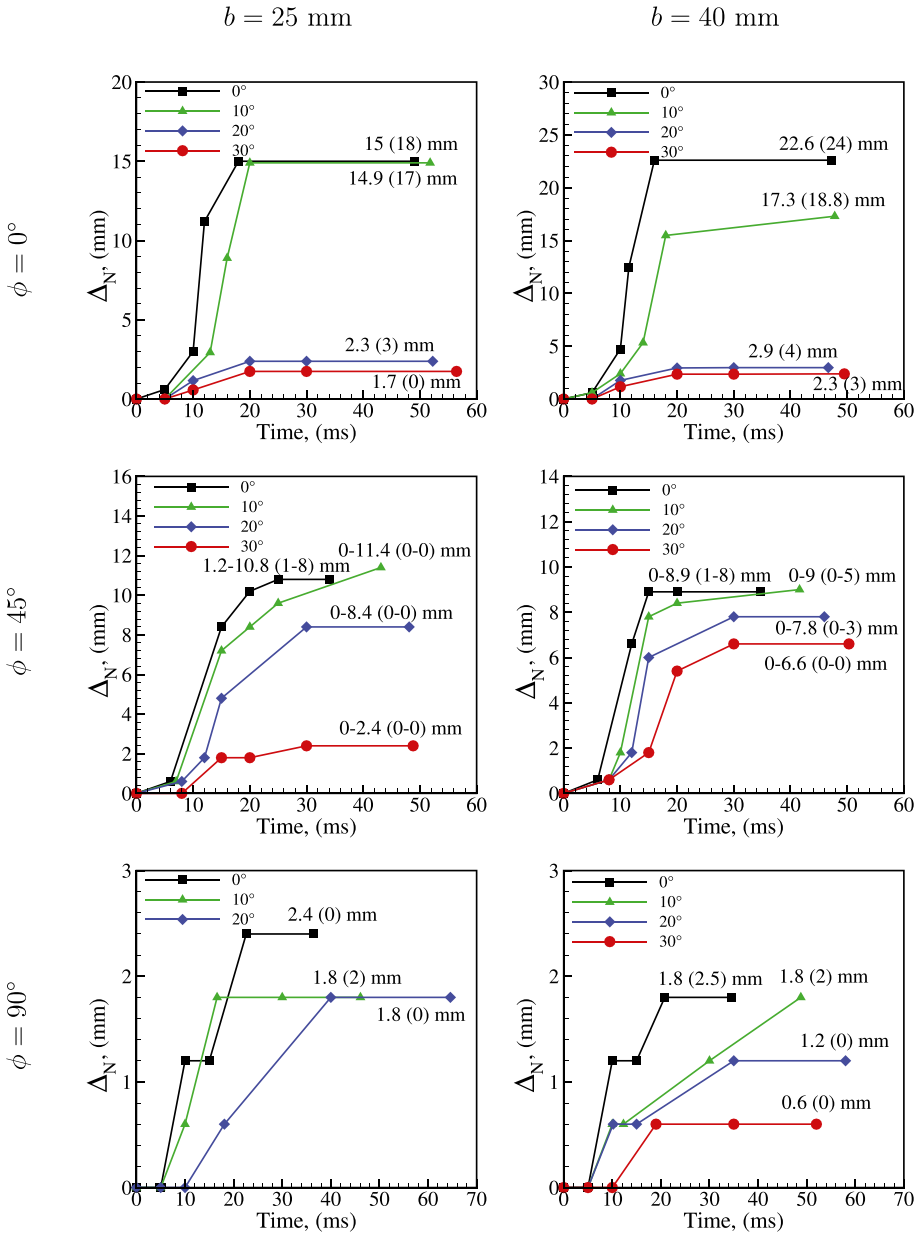


**Fig. 12** Time dependent adhesive damage propagation for different impact angles. ( $\Delta_{N'}$ : numerical axial separation length,  $\phi$ : fiber angle,  $b$ : overlap length)

slowed down. Axial separation in the joint with 40 mm overlap length and  $10^\circ$  impact angle propagated with a very small increase after 20 ms. Adhesive damage propagation rate decreased with the increase in impact angle for the joints with  $0^\circ$  fiber angle. Axial separation value for the joints with  $45^\circ$  fiber angle showed a rapid increase in the time interval of 0–30 ms and after this period, there was a slight increase in damage propagation. In addition to adhesive damage in the joints with  $45^\circ$  fiber angle, composite damage also occurred. Therefore, the adhesive damage propagation rate was slower than the joints with  $0^\circ$  fiber angle, and it caused a decrease in the amount of adhesive damage. The increase in overlap length increased the load-carrying capacity of the joints. Experimental and numerical axial separation values increased with increasing overlap length for the joints with  $0^\circ$  fiber angle. In the joints with  $45^\circ$  fiber angle, except for the joint with  $30^\circ$  impact angle, the increase in overlap length caused a decrease in the axial separation value. Matrix shear damage occurred in the region close to the free edges of the overlap region for the joints with  $90^\circ$  fiber angle under impact load. In addition to the composite damage, a very small amount of adhesive damage was observed in the numerical result. Increasing impact angle and fiber angle had a significant effect on the adhesive damage area and adhesive damage propagation rate in the joints.

## 6 Damage Development in Composite Adherends

The damage initiation and propagation in composite adherends of single-lap joints under impact load were determined by Hashin's damage criterion. Damage types in composite adherends were evaluated by Hashin's fiber tensile (FT), fiber compression (FC), matrix tensile (MT), matrix compression (MC), and matrix shear (MS) damage criteria. Tensile fiber damage, compressive fiber damage, tensile matrix damage, compressive matrix damage, and shear matrix damage were determined by DAMAGEFT, DAMAGEFC, DAMAGEMT, DAMAGEMC, DAMAGESHR damage index, respectively. The impactor was in contact with the 4th layer of the top composite adherend (Fig. 2). The damage level is indicated with a damage index varying between 0 and 1, which is calculated separately for each damage criterion of the composite adherends. A value of 0 indicates that no damage occurred in the composite material, and a value of 1 indicates that the composite material was damaged. The damage distributions of composite adherends for the joints with  $0^\circ$  fiber angle and 25 mm overlap length are shown in Fig. 13. Composite damage in the joints occurred in the ply-1 (bottom), ply-3 (top), and ply-4 (top). No damage was observed in other composite plies. Fiber compression (FC) and matrix shear (MS) damage were detected for joints with  $0^\circ$  fiber angle.

The joints with  $0^\circ$  fiber angle have the highest bending strength. Therefore, low-level composite damage occurred in the joints. Matrix shear and fiber compression damage were more intense in the first layer (ply-4) that the impactor contacted, while they decreased towards the lower plies. The increase of overlap length did not significantly affect the damage development in composite adherends. The damage distributions and damage areas of composite adherends of the joints with  $45^\circ$  fiber angle are shown in Fig. 14. Fiber compression (FC), matrix compression (MC), matrix tensile (MT), and matrix shear (MS) damage types were determined in the joints with  $45^\circ$  fiber angle. The fiber compression damage type occurred only in ply-4, where the impactor and the upper composite adherend were in contact. Damage areas were calculated for damage variable values of 0.9 and above



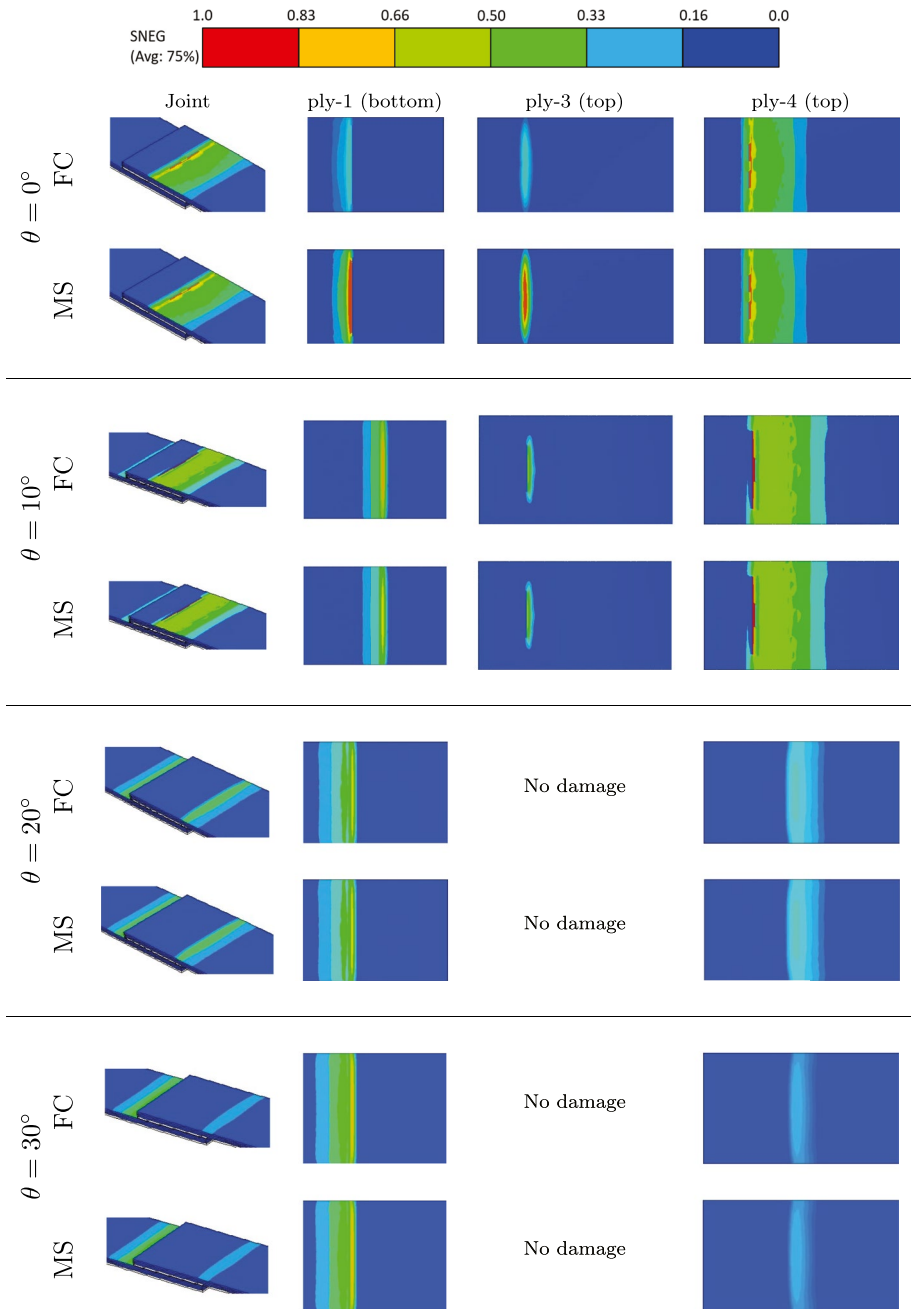
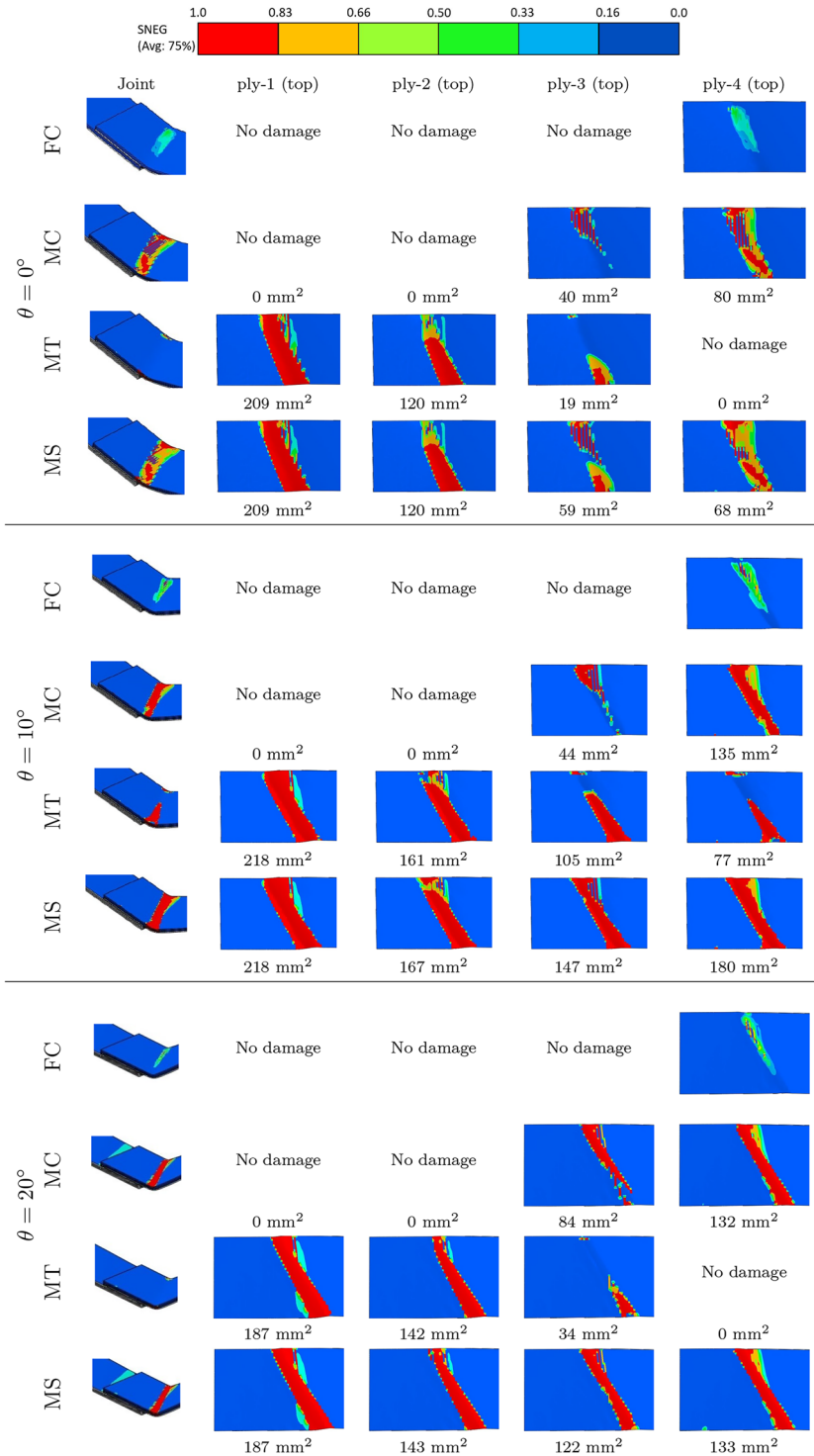


**Fig. 13** Damage types and distributions according to different damage criteria in the plies of the top and bottom composite adherends for joints with  $0^\circ$  fiber angle and 25 mm overlap length ( $\theta$ : impact angle)



◀**Fig. 14** Damage types and distributions according to different damage criteria in the plies of the top and bottom composite adherends for joints with 45° fiber angle and 25 mm overlap length ( $\theta$ : impact angle)

(red zone). Torsional moment, due to an unbalanced joint caused shear damage in the composite and adhesive. Composite damage occurred predominantly in the matrix material. Matrix tensile, matrix compression, and matrix shear damage occurred along the fiber direction. In joints with 25 mm overlap length, the damage occurred in the plies of the top composite adherend for 0°, 10°, and 20° impact angles, while the damage occurred in the bottom composite adherend plies at the 30° impact angle. Matrix shear damage was more dominant than other damage types in these composite plies. The increase in the impact angle caused a changing damage mechanism and decreased the damaged area. Increasing in-plane shear stress with increasing impact angle caused matrix shear damage. While the matrix shear damage area was lower in the 4th ply of the top composite adherend, the matrix shear damage area in the composite plies increased towards the adhesive region. As a result of the unbalanced joint type, the rotational moment along the longitudinal axis increased the effect of shear stress in the adhesive-composite interface. Matrix tensile and matrix shear damage types were the dominant damage types in the joints with 45° fiber angle. While these two damage types were more active in the plies around the top composite-adhesive interface, the damage area decreased towards the composite ply in contact with the impactor. The unsymmetrical structure caused the matrix tension, matrix compression, and matrix shear damage to dominate in the plies of the composite adherend. The most damage area occurred in the matrix shear damage type for all impact angles and the matrix shear damage was the dominant damage type. The highest matrix shear damage area occurred in the ply-1 (top) for all impact angles with the increasing effect of shear stress. Adhesive damage also occurred in the upper composite-adhesive interface region close to this region. In the ply-1 (top), matrix tensile damage was as effective as shear damage. The fracture toughness of the adhesive in the normal direction is lower than the shear toughness. The high tensile stress in the overlap region caused adhesive damage.

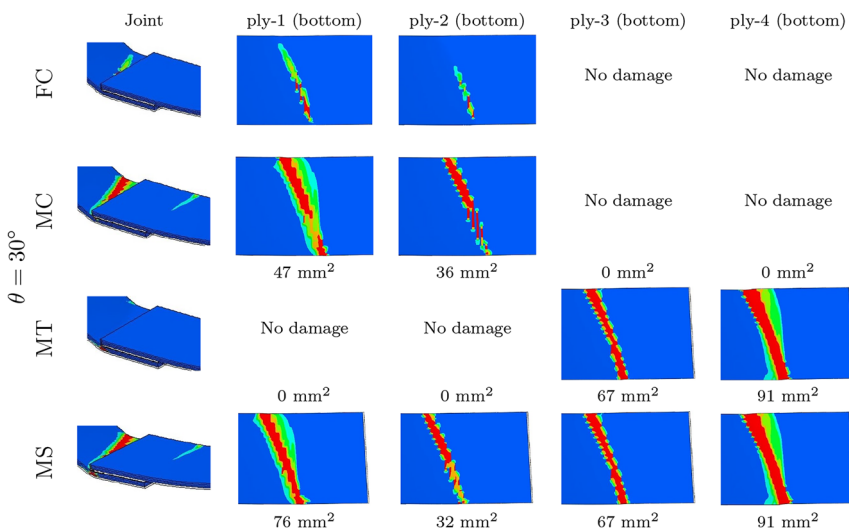
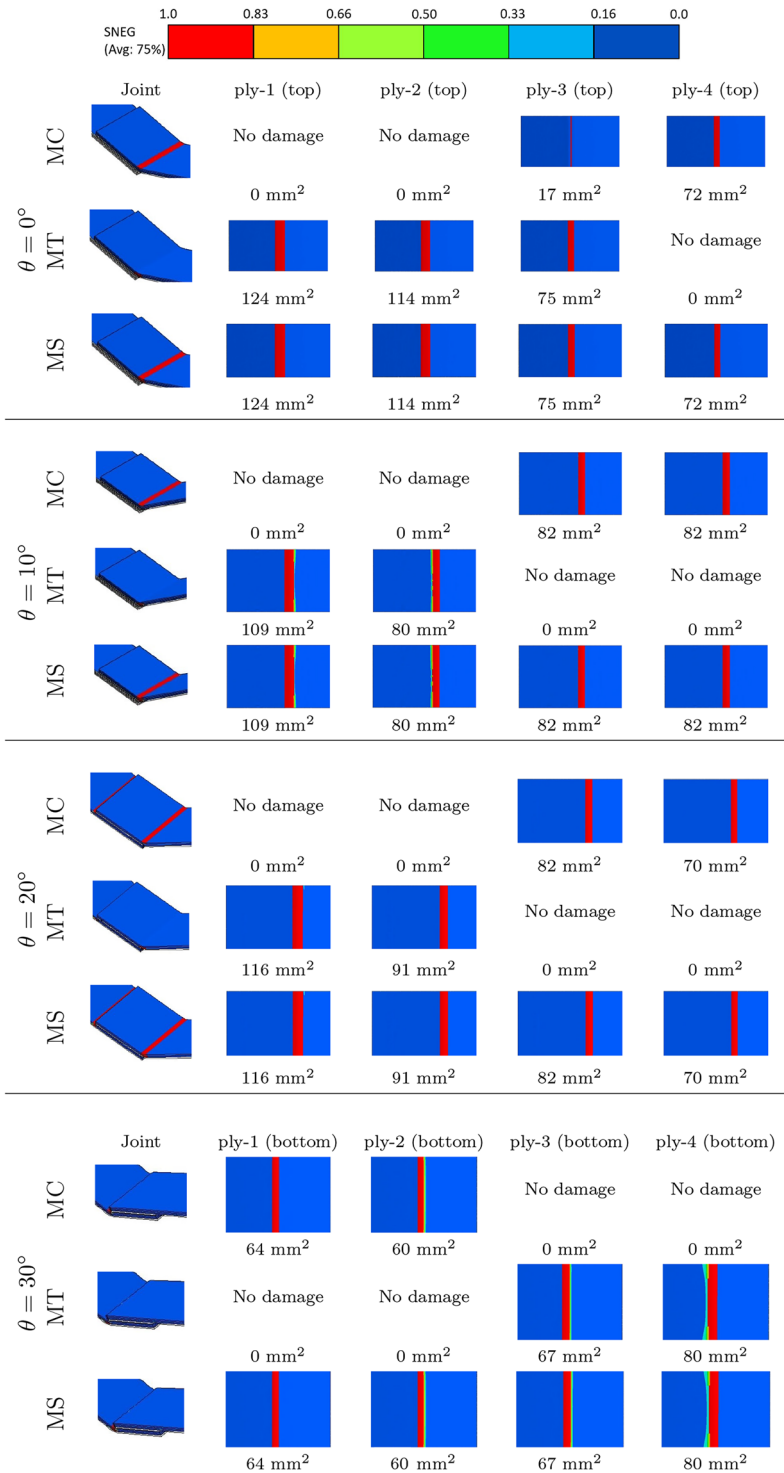


**Fig. 14** (continued)



◀**Fig. 15** Damage types and distributions according to different damage criteria in the plies of the top and bottom composite adherends for joints with 90° fiber angle and 25 mm overlap length ( $\theta$ : impact angle)

Since the unbalanced joint was forced to rotate around its axis, the effect of the tensile stress decreased from ply-1 (top) to ply-4 (top), while the effect of the compressive stress increased. As a result, while the matrix tensile damage area reached the highest value in ply-1 (top), the matrix compression damage area was the highest in ply-4 (top). Unbalanced in-plane shear stress caused matrix shear damage in all top composite plies.

The damage distributions and damage areas of the composite adherends for the joints with 90° fiber angle, which has the weakest bending strength compared to the other two joint types, are shown in Fig. 15. In the joints with 90° fiber angle, the impact load was covered by the matrix and adhesive materials. For all impact angles, shear (matrix) damage occurred at the free edges of the overlap zone. The damage types detected in the joints were Matrix Compression (MC), Matrix Tensile (MT), and Matrix Shear (MS) damage. The damage types that occurred in the upper composite adherend with the increase in the impact angle were also detected in the lower composite adherend. With the increase in the impact angle, the bottom composite adherend was also damaged. The highest damage area occurred at 0° impact angle. Matrix shear damage was more dominant than other damage types. Shear damage was greater in ply-1 (top). The matrix compression damage became evident after ply-2 (top) and the matrix tensile damage area decreased from ply-1 (top) to other plies. The free edge of the overlap region was under a severe bending moment with impact load and this bending moment caused matrix damage. In the experimental study, joints with 90° fiber angle suffered shear damage around the free edges of the overlap region. There is a good agreement between the experimental and numerical composite damage types and distributions.

## 7 Conclusions

The mechanical behavior of adhesively bonded composite single-lap joints under low-speed impact was numerically investigated. The effects of impact angle, fiber orientation, and overlap length on the impact behavior of the adhesive joints were investigated comparatively. The agreement between the developed numerical model and the experimental results was evaluated. In addition, composite and adhesive damage were examined in detail. The main results obtained in this study are as follows:

- The developed numerical model predicted both the impact behavior of the composite single-lap joints and the damage types of adhesive and adherends close to the experimental results. Using both the CZM and the elastic–plastic material model in the adhesive numerical model enabled the reflection of the plastic deformation ability of the adhesive as well as the determination of the damage initiation and propagation in the adhesive region.
- Composite fiber orientation and impact angle had a significant effect on the impact behavior of composite single-lap joints. The increase in fiber angle and impact angle caused a decrease in the maximum contact force value. In addition, with the increase in the impact angle, the surface area in contact with the impactor increased and therefore the total contact time increased.

- The adhesive damage pattern varied depending on the fiber orientation of the composite adherends. For the joints with  $0^\circ$  and  $45^\circ$  fiber angles, adhesive damage propagated along the fiber direction. In addition, the composite fiber orientation also had an effect on the adhesive damage propagation rate. Adhesive damage initiated earlier and propagated faster for the joints with  $0^\circ$  fiber angle. The impact angle affected the adhesive damage propagation rate. As the impact angle increased, the adhesive damage propagation rate decreased. Moreover, the amount of adhesive damage decreased as the impact angle increased, since the adhesive material was more resistant to shear stress.
- Matrix tensile damage and matrix shear damage were the predominant types of composite damage in the joints with  $45^\circ$  and  $90^\circ$  fiber angles. In the joints with  $0^\circ$  fiber angle, the amount of the composite damage was low as the impact energy was covered by the adhesive damage. However, considerable composite damage occurred at the free edges of the overlap region in the joints with  $45^\circ$  and  $90^\circ$  fiber angles.

**Funding** The research in this paper was financially supported by the Scientific Research Project Division of Erciyes University under contract FDK-2017-7318.

**Data Availability** According to the protocol (FDK-2017-7318) signed among Authors and Presidency of Erciyes University, the full or partial use of all numerical analysis results in this study is subject to permission from Presidency of Erciyes University. Authors hold this permission to publish the journal article.

## References

1. Da Silva, L.F., Dillard, D.A., Blackman, B., Adams, R.D.: Testing adhesive joints: best practices. John Wiley & Sons (2012)
2. da Silva, L.F.M., Pirondi, A., Öchsner, A.: Hybrid adhesive joints, p. 309. Springer Science & Business Media Berlin Heidelberg (2011)
3. Adams, R.D., Comyn, J., Wake, W.C.: Structural adhesive joints in engineering, p. 359. Chapman & Hall London (1997)
4. Da Silva, L.F., Öchsner, A., Adams, R.D.: Handbook of adhesion technology, p. 1554. Springer Science & Business Media Verlag Berlin Heidelberg (2011)
5. Machado, J.J.M., Marques, E.A.S., da Silva, L.F.M.: Adhesives and adhesive joints under impact loadings: An overview. *J. Adhes.* **94**(6), 421–452 (2018)
6. Chen, C., Sun, C., Han, X., Hu, D., Zhou, J., Guan, Z.: The structural response of the thermoplastic composite joint subjected to out-of-plane loading. *Int. J. Impact Eng* **145**, 103691 (2020)
7. He, B., Pan, Y.: Failure mechanism of single lap, adhesively bonded composite-titanium joints subjected to solid projectile impact. *J. Adhes. Sci. Technol.* **36**(4), 370–391 (2022)
8. Anderson, T.L.: Fracture mechanics: fundamentals and applications. CRC press (2017)
9. Hazimeh, R., Challita, G., Khalil, K., Othman, R.: Finite element analysis of adhesively bonded composite joints subjected to impact loadings. *Int. J. Adhes. Adhes.* **56**, 24–31 (2015)
10. Machado, J., Gamarra, P.-R., Marques, E., da Silva, L.F.: Numerical study of the behaviour of composite mixed adhesive joints under impact strength for the automotive industry. *Compos. Struct.* **185**, 373–380 (2018)
11. Morgado, M., Carbas, R., Dos Santos, D., Da Silva, L.: Strength of cfrp joints reinforced with adhesive layers. *Int. J. Adhes. Adhes.* **97**, 102475 (2020)
12. Machado, J., Nunes, P., Marques, E., da Silva, L.F.: Numerical study of similar and dissimilar single lap joints under quasi-static and impact conditions. *Int. J. Adhes. Adhes.* **96**, 102501 (2020)
13. Peres, L., Arnaud, M., Silva, A., Campilho, R., Machado, J., Marques, E., dos Reis, M., Da Silva, L.: Geometry and adhesive optimization of single-lap adhesive joints under impact. *J. Adhes.* **98**(6), 677–703 (2022)
14. Araújo, H., Machado, J., Marques, E., Da Silva, L.: Dynamic behaviour of composite adhesive joints for the automotive industry. *Compos. Struct.* **171**, 549–561 (2017)

15. Hu, C., Huang, G., Li, C.: Experimental and numerical study of low-velocity impact and tensile after impact for CFRP laminates single-lap joints adhesively bonded structure. *Materials* **14**(4), 1016 (2021)
16. Huang, W., Sun, L., Li, L., Shen, L., Huang, B., Zhang, Y.: Investigations on low-energy impact and post-impact fatigue of adhesively bonded single-lap joints using composites substrates. *J. Adhes.* **96**(15), 1326–1354 (2020)
17. Liu, B., Yan, R.: Damage mechanism and residual strength at different impact locations for composite bonding scarf repairs. *J. Adhes. Sci. Technol.* **32**(23), 2523–2536 (2018)
18. Erbayrak, E.: Investigations of low-velocity impact behaviour of single-lap joints having dissimilar hybrid composite adherends through cohesive zone model approach. *J. Adhes. Sci. Technol.* **36**(5), 545–565 (2022)
19. Boling, H., Dongyun, G.: Dynamic analysis of single-lap, adhesively bonded composite-titanium joints subjected to solid projectile impact. *J. Adhes. Sci. Technol.* **32**(11), 1176–1199 (2018)
20. Atahan, M.G., Apalak, M.K.: Low-speed bending impact behavior of adhesively bonded single-lap joints. *J. Adhes. Sci. Technol.* **31**(14), 1545–1575 (2017)
21. Atahan, M.G., Apalak, M.K.: Low-speed bending impact behaviour of adhesively bonded dissimilar single-lap joints. *J. Adhes. Sci. Technol.* **36**(16), 1794–1822 (2022)
22. Atahan, M.G., Apalak, M.K.: Experimental investigation of oblique impact behavior of adhesively bonded composite single-lap joints. *Appl. Compos. Mater.* **29**(3), 1293–1319 (2022)
23. Zhang, C., Huang, J., Li, X., Zhang, C.: Numerical study of the damage behavior of carbon fiber/glass fiber hybrid composite laminates under low-velocity impact. *Fibers Polym.* **21**, 2873–2887 (2020)
24. Zhang, T., Yan, Y., Li, J.: Experiments and numerical simulations of low-velocity impact of sandwich composite panels. *Polym. Compos.* **38**(4), 646–656 (2017)
25. Araldite 2015 epoxy adhesive, Huntsman Advanced Materials. <http://www.huntsman.com>. Accessed 4 Apr 2023
26. Yildirim, M., Apalak, M.K.: Transverse low-speed impact behavior of adhesively bonded similar and dissimilar clamped plates. *J. Adhes. Sci. Technol.* **25**(1–3), 69–91 (2011)
27. ABAQUS, Analysis user's guide documentation version 6.13, Dassault Systems SIMULIA Corp (2013)
28. Matzenmiller, A., Lubliner, J., Taylor, R.: A constitutive model for anisotropic damage in fiber-composites. *Mech. Mater.* **20**, 125–152 (1995)
29. Hashin, Z., Rotem, A.: A fatigue failure criterion for fiber reinforced materials. *J. Compos. Mater.* **7**(4), 448–464 (1973)
30. Hashin, Z.: Failure criteria for unidirectional fiber composites. *J. Appl. Mech.* **47**, 329–334 (1980)
31. Camanho, P.P., Dávila, C.G.: Mixed-mode decohesion finite elements for the simulation of delamination in composite materials, pp. 1–37. NASA/TM-2002-211737 (2002)
32. Campilho, R.D., Banea, M.D., Neto, J., da Silva, L.F.: Modelling adhesive joints with cohesive zone models: effect of the cohesive law shape of the adhesive layer. *Int. J. Adhes. Adhes.* **44**, 48–56 (2013)
33. Moreira, R.D., de Moura, M.F., Silva, F.G., Rodrigues, J.S., Silva, F.D.: Fracture characterization of a bi-material bonded aluminum/CFRP joints under mixed-mode I+II loading. *Fatigue Fract. Eng. Mater. Struct.* **45**(8), 2215–2226 (2022)
34. Wong, K.J.: Moisture absorption characteristics and effects on mechanical behaviour of carbon/epoxy composite: application to bonded patch repairs of composite structures. PhD thesis, Dijon (2013)
35. Kaddour, A., Hinton, M.J., Smith, P.A., Li, S.: Mechanical properties and details of composite laminates for the test cases used in the third world-wide failure exercise. *J. Compos. Mater.* **47**(20–21), 2427–2442 (2013)
36. Aktaş, M., Karakuzu, R.: Determination of mechanical properties of glass-epoxy composites in high temperatures. *Polym. Compos.* **30**(10), 1437–1441 (2009)
37. İcten, B.M., Atas, C., Aktas, M., Karakuzu, R.: Low temperature effect on impact response of quasi-isotropic glass/epoxy laminated plates. *Compos. Struct.* **91**(3), 318–323 (2009)
38. Lapczyk, I., Hurtado, J.A.: Progressive damage modeling in fiber-reinforced materials. *Compos. A Appl. Sci. Manuf.* **38**(11), 2333–2341 (2007)

**Publisher's Note** Springer Nature remains neutral with regard to jurisdictional claims in published maps and institutional affiliations.

Springer Nature or its licensor (e.g. a society or other partner) holds exclusive rights to this article under a publishing agreement with the author(s) or other rightsholder(s); author self-archiving of the accepted manuscript version of this article is solely governed by the terms of such publishing agreement and applicable law.